Large eddy simulations of a piston-driven high-speed synthetic jet

A thesis submitted in fulfillment of the requirements

for the degree of Doctor of Engineering

PHAM Duy Tung

Fluid Dynamics Laboratory

Department of Aerospace Engineering

Graduate School of Engineering

Nagoya University, Japan

August 2023

Dissertation Committee

Associate Professor

WATANABE Tomoaki

Professor

TSUJI Yoshiyuki

Professor

KASAHARA Jiro

Professor

NAGATA Koji

ACKNOWLEDGEMENT

Firstly, I would like to express my sincere gratitude to my supervisors, Professor NAGATA Koji and Professor WATANABE Tomoaki, for instructions, and for giving me motivation with much patience during my study. It was an honor to achieve my Ph.D. journey under their supervision.

I would also like to thank Professor TSUJI Yoshiyuki and Professor KASAHARA Jiro for their invaluable comments on my thesis. Their meaningful recommendations further improved this thesis.

I want to take this opportunity to express my appreciation to all the students in our laboratory, who has helped me from the first day I became a member of the Fluid Dynamics Laboratory.

This thesis would not be possible without the support and understanding of my family and my wife. I am grateful for their encouragement, patience, and never-ending love.

Finally, I am grateful to the LGS program for financial support and warm encouragement during my academic study.

PHAM Duy Tung, August 2023

TABLE OF CONTENT

LIST OF PUBLISHED PAPERS

Chapter 2

Tung, P. D., Watanabe, T., & Nagata, K. (2023). Large-Eddy Simulation of a Flow Generated by a Piston-driven Synthetic Jet Actuator. *CFD Letters*, 15(8), 1–18. https://doi.org/10.37934/cfdl.15.8.118

Chapter 3

Tung, P. D., Watanabe, T., & Nagata, K. (2023). LES Investigation of a Piston-driven Synthetic Jet Actuator with Multiple Orifices, *CFD Letters*, Accepted, 2023/6

LIST OF FIGURES

LIST OF TABLES

CHAPTER 1. INTRODUCTION

1.1. Background

Controlling flow usually uses two strategies, which are passive and active methods. Going back in time, Prandtl [1] first introduced boundary layer theory and used it for flow control. Substantial developments followed this in flow control for the development of the aviation industry. One of the control techniques are examined with the aim of achieving delayed transition, postponed separation, enhanced lift, reduced drag, increased turbulence, or suppressed noise [1]. The passive method is provided with changes in geometries, for example, vortex generators (VGs), as shown in Figure 1.1. Implementing VGs is highly effective in generating a substantial boost not only in the maximum lift coefficient but also in the static stall angle of attack for the airfoil with a blunt trailing edge. In addition, VGs demonstrate remarkable effectiveness in mitigating the separation caused by shock waves [2]. Nevertheless, employing VGs comes at the cost of a decreased lift-to-drag ratio [3]. To address this issue, the ideal solution often entails modifying the proportion between the height of VGs and the wing chord [4]. This optimization aims to enhance the stall angle and maximize the lift coefficient while minimizing drag.

Nevertheless, the effectiveness of active flow control relies on the implementation of actuators, which necessitate extra energy. It can be effectively combined with sensors and a feedback loop to detect separation flow. The system combining a hybrid array of Micro Electro Mechanical Systems (MEMS) wall double hot wires with higher sensor density on the top surface of the flap is highly efficient in accurately detecting trailing edge separation [5].

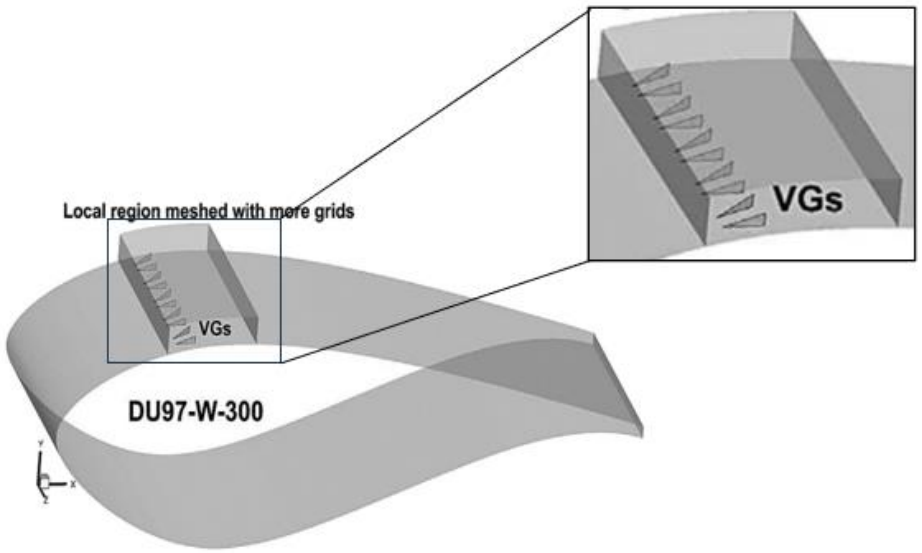

Figure 1.1. Geometry of airfoil with VGs [3].

In active control, actuators such as fluidic devices, moving objects, plasma, or electromagnetic mechanisms are frequently employed [6]. These approaches inevitably involve inherent trade-off in terms of fabrication methods, design optimization or system-level robustness.

A notable instance of active control is the use of a plasma actuator, which encompasses technologies like dielectric barrier discharge (hereinafter referred to as “DBD”) [6]. The plasma actuator offers several benefits due to its uncomplicated structure devoid of moving components and rapid responsiveness. For flow control of an airfoil, it utilizes an uneven configuration of a pair of electrodes, leading to increased lift and reduced drag coefficients [7] [8]. The use of DBD with full-scale unmanned air vehicle can improve the lift coefficient up to 0.6 [9].

Efforts to enhance DBD plasma actuators are ongoing, focusing on refining their design aspects. They can be applied voltage and pulsed frequencies [10] [11]. About the dielectric thickness, it has a significant effect on increasing body force [12]. A thick one is better than a thin one. However, ranging from 0.5 to 5 mm, the maximum velocity of electric wind is independent with the thickness [13].

In recent studies, they are examined how the size of vortices is affected by pulsed actuation and compared the improvements achieved through pulsed actuation with the gradual actuation counterpart. Nonetheless, these DBD plasma actuators produced the induced flow, which is generally sluggish. On the other hand, the conventional flow velocities around actual airfoils are either supersonic or transonic. Above a DBD actuator, the velocity histories observed and the streamwise velocity is maximized, but it is below 6.0 m/s across various scenarios involving different voltages and configurations, including single actuators, dual actuators, and triple actuators [12] [13] [14]. By utilizing the 30 kW of voltage, the DBD plasma actuator generates the velocity of the ionic wind, which can reach a velocity of 7.1 m/s [15] but not over 8 m/s [16]. As a result, the velocity spectrum of jets generated by traditional synthetic jet actuators (hereinafter referred to as “SJAs”) and DBD plasma actuators is inadequate for managing flows at high speeds.

Another commonly used technique in flow control within the fluidic field involves the utilization of piezoelectric SJAs equipped with a membrane vibrating. The oscillation of the driver developed the vortex pair [17], as shown in Figure 1.2, and turbulent jet in downstream region. In the many investigations, synthetic jets have been studied because of their unique property, which is formed entirely from working fluid [18].

The synthetic jet is often generated with a piezoelectric driver, which has been used to study the fundamental factors in the synthetic jet form and behavior, such as the vortex pair [17]. Comparisons of synthetic jets with continuous jets are also reported in previous studies. For example, with the same Reynolds number (2000), although the mean velocity profiles between them are similar, the synthetic jets are wider in width [19]. However, the acceleration and deceleration of the synthetic jet influences the instant velocity profile and the probability density function (PDF) of the velocity time derivative. Therefore, they are different from continuous jets [20]

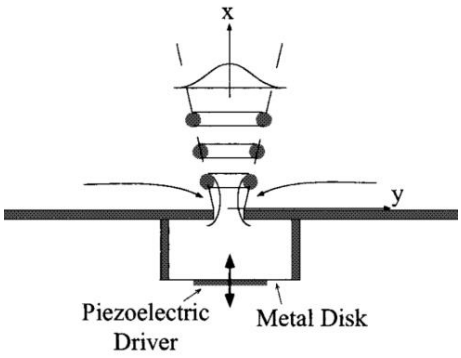

Figure 1.2. Piezoelectric synthetic jet [17].

The substantial enhancement of the jet proves to be successful in actively manipulating the boundary layer [21]. In flow control, the synthetic jet has been demonstrated effectively by altering vorticity and velocity's distribution [18]. Due to the heat transfer properties associated with turbulence, synthetic jet actuators are also utilized as cooling devices [22] [23]. Therefore, multi-orifice synthetic jet also has advantages in heat transfer rate compared with single-orifice jet [24].

In another application, synthetic jets show potential application in flow control [25]. In aerodynamics, it can delay flow separation on airfoils by reducing the surface

boundary layer thickness. Synthetic jet is often utilized to generate turbulence with targeted properties, such as isotropic turbulence without a mean flow in fundamental studies of turbulence [26]. A random nine-synthetic-jet system can generate turbulence with large velocity fluctuations and a small mean flow [27].

Furthermore, synthetic jet has the capability to significantly enhance the lift/drag ratio of a 2D cylinder [28]. Using the piezoelectric actuator, it created the strong entrainment to delay separation [29]. In a state of coupled resonance of the diaphragm and cavity are, SJAs achieved a peak efficiency. In gas turbine combustors, by leveraging the wake structure, the flow mixing is improved by SJAs at dissimilar temperatures [30]. Using SJAs, to examine the regulation of separated flows in dissipation, Lyubimov and Potekhina performed numerical simulations [31]. Testing with two types of synthetic jet, the tangential jet aids in suppressing flow separation and delaying airfoil stall. It increases the flow's velocity within the inner boundary layer and adds energy. On the other hand, the normal jet improves the mixing of flows between the inner and outer boundary layers. By this way, the boundary layer is thickened. Furthermore, the drag coefficient is reduced with the airfoil. This phenomenon occurs mainly when the momentum coefficient of the synthetic jet is relatively low [32]. By improving and applying the force in oscillation at 19.7 kHz, the vibrating surface can create a jet with a velocity exceeding 100 m/s. In addition, the energy consumption is extremely low, with a few mJ per pulse [33] .With features that can be applied to flow control for airfoil, however, piezoelectric synthetic jet also has certain disadvantages affecting jet performance. One of the first disadvantages is that, with the power limitation for the membrane, the ratio between the cavity size without displacement and the minimum size of the cavity when the displacement is

maximum, i.e., volumetric displacement is not large enough to create a large enough pressure, resulting in not being able to increase the velocity at the orifice exit [34]. In addition, it is related to the membrane material and the frequency limit. These have affected the upper limit of the generated jet velocity.

In active flow control, piston-driven synthetic jets are one of the methods used to overcome above problems. The device generates a synthetic jet using an up-and-down of a piston within a cylinder. This motion creates pressure fluctuations, leading to the formation of a synthetic jet. Comparing to other methods, it is characterized by its robustness in producing high-velocity jet flow and active control. Therefore, it plays a crucial role in achieving specific aerodynamic effect by manipulating the flow of air around the airfoil at higher flying speed.

1.2. Jets interaction

The interaction of multiple continuous jets results in a complex flow field. An array of holes can be used to generate multiple jets for possible technical applications or further study. For example, four aligned jets are ejected within the boundary layer to reduce drag in film cooling [35]. Nasr et al. [36] divide the jet interaction regions by converging, merging, and combining regions. The maximum of the mean streamwise velocity is reached at the combined point in the x direction [36]. Ghahremanian et al. investigated a confluent jet array and confirmed that the velocity at which the jets merge is lower than a twin jet, but the mean velocity decay is slower [37]. For the jet interaction, there are also linear relationships between the nozzle spacing extension and the streamwise location of the combining/merging points [38], and between the separation length and the merging point location [39]. The jet spacing also has a significant influence on the production of vortices [40]. Theoretical power laws for kinetic energy spectra of turbulence are often observed in a single turbulent jet [41]. It is also evaluated in the interaction regions of multiple jets [42]. The interaction results in the non-Kolmogorov -5/3 spectrum of streamwise velocity fluctuations [43]. In addition, the relationship between extreme events and the -5/3 law is proved for the jet interaction [44].

Regarding the interaction of multiple synthetic jets, Smith et al. showed that the phase angle affects the path of the newly merged vortex pair due to the strong entrainment of ambient fluid [45]. With a modified design, the incline synthetic jet array can attain a peak velocity of up to 100 m/s [46]. Jankee et al. showed that the multiple synthetic jets are efficient in separation control and drag reduction when the

orifice spacing is smaller than 6.5 times the orifice diameter [47]. In addition, at a high vibration amplitude, the large opening angle of the orifice largely affects the performance [23]. Coupling with the cross-flow of 14.7 m/s and 8 m/s, the activation of the synthetic jet array contributes up to 9.3 % and 23.1 % of the heat transfer coefficient, respectively [48].

1.3. Some previous studies about piston synthetics jets

Piston synthetic jet (PSJ) is in the synthetic jet class. With the difference coming from the structure of the piston compared to the membrane types, it can produce a jet at high speed. At the same time, the durable system offers high application potential.

With conventional synthetic jets, there are some limitations related to the frequency of oscillations, the material for the diaphragm, and even the power input. These limitations have been significantly overcome through the development of piston synthetic jet actuators (PSJAs [(*)]), which can provide a high-speed regime [34]. It can achieve full-scale application when the peak velocity reaches 124 m/s [49]. One of those specific applications is an application to an airfoil [50]. By using PSJA, the highest lift coefficient ascends by 80%, and the stall angle changes from 12 to 18 deg. [50]. With higher angles of attack, PSJA is incredibly effective. In another experiment in understanding the temperature-variation effect of PSJ, it was also confirmed that the temperature increased significantly even in the cavity, and significantly increased compared to ambient temperature [51]. The heat transfer coefficient rises as the frequency is raised. When considering a specific frequency, in determining heat transfer, the size of the orifice is one of essential parameters. As the diameter decreases leading to the increasing of heat transfer [52].

In one of the latest experiments with PSJ of the single orifice, the velocity of flow can reach approximately Mach 1.6 [53]. Crittenden et al. [34] studied the parameters affecting the velocity characteristics, including compression ratio, actuation frequency and piston stroke length. The compressibility effect relates to the

pressure asymmetry during the suction and blowing phases. In addition, there is a correlation between the maximum Mach number and the maximum pressure inside the actuator [53]. This correlation is also found in a numerical model.

Regarding the fundamental study of the properties of PSJ, the original experiment was performed by Crittenden with the piston structure shown in Figure 1.3. The pressure transducer was assembled at the top plate to measure the pressure histories in each condition. Due to the compressibility effect, the profile shape of pressure is different between the blowing and suction phases. The critical parameters affecting PSJ performance are confirmed. They are compression ratio, frequencies, stroke length [34].

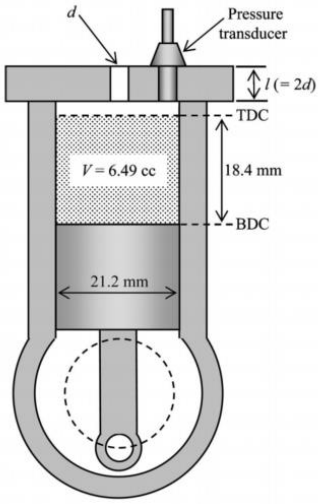

Figure 1.3. Schematic diagram of piston synthetic jet [34].

With a similar experimental system structure, Sakakibara [53] has continued to develop with the single/multi-orifice jets model. Jet flow is visualized by shadowgraph. In addition, a correlation relationship between maximum Mach number and maximum pressure is found. At the same time, the study also showed the dependence of extremum of pressure during each cycle on the total orifice area. One

of the improvements that changed PSJ was structurally when Eri [54] developed the experiment with the auxiliary air inlet. This inlet is located at the bottom of the cylinder. That leads it to open automatically when the piston moves down and over; when the piston moves up, the inlet closes. With a significant increase in suction capacity, the increase in mass flow contributes mainly to the increase in cylinder pressure and jet velocity.

By the interacting of supersonic synthetic jets, compressible turbulence is generated by the PSJs. The compressible turbulence chamber was developed with the opposition of the jet arrays, which generates nearly homogeneous and isotropic turbulence with a small mean velocity at the chamber center [55]. Furthermore, the compressible homogeneous and isotropic turbulence generated by the PSJAs was investigated to evaluate compressibility effects on the statistical properties of turbulence [56].

Although high-speed synthetic jets generated from multiple orifices of PSJs have potential applications for flow control and fundamental studies of turbulence, such flows have hardly been investigated. Sakakibara et al. [53] characterized the performance of the PSJA with two or four orifices with the pressure measurement inside the actuator and flow visualization. However, the flow field formed by the interaction of the multiple synthetic jets has not been investigated in detail.

(*) SJA is a device that generates a conventional synthetic jet, while PSJA is a device driven by a piston that generates a piston-driven synthetic jet.

1.4. Previous model for synthetic jets

A remarkable survey by large eddy simulation of OpenFOAM by Ziade et al. [57] shows correlation of cavity shape to flow at an orifice outlet. To explain the phenomenon, a detailed simulation of the cavity was conducted. By a commercial code, for the case of a conventional synthetic jet, it is show that the frequency causes a greater dependence on SJ than the amplitude [58]. Regarding the method of meshing for the moving piston, the dynamic mesh is also more reasonable than the velocity method [59]. In addition, direct simulation can also use for the synthetic jet by compressible equations [60]. For the jet interaction, a RANS model is employed, and the direction of the merged jets depends on the initial phase with a significant relative phase of the two jets [61].

Another application of the synthetic jet array is utilized for the enhancement of heat transfer in the heat sinks for electronics cooling. Cavity size, shape, and orifice length are parameters that affect heat transfer performance [22]. The cooling of the plate is more effective in the blowing phase with increasing turbulence levels [62].

1.5. The object of research

Through the above studies, the key focus of this research lies in studying the flow field of single/ multiple PSJ in details, which has not investigated. In addition, the pressure histories within the cylinder are analyzed, as it is one of the critical parameters associated with this particular type of synthetic jet. The influencing parameters and properties of PSJ are also considered.

In the case of multi-orifice jets, pressure histories have continued to be essential and well-studied information. At the same time, the relationship between pressure and orifice area was confirmed to be mutually influential. Furthermore, information about jet interactions is still needed. For multi-orifice jets, in the case of only two orifices, how would this interaction be? As for the possibility of more than two orifices, what will be the intersection region among PSJs? Currently, the parameters for these phenomena still need to be understood.

Understanding these characteristics is essential for basic research and practical applications.

In the scope of this thesis, a computational model is developed to investigate the properties of both single-orifice and multi-orifice jets thoroughly. The primary objective of this model, based on empirical dimensions, is to bridge the knowledge gap by filling in the missing information concerning the specific characteristics of PSJ. This computational approach aims to provide comprehensive insights and answers to the pertinent questions that arise in the study of PSJ, unraveling its unique properties and behavior. These studies contribute to the current understanding and knowledge in this field of research.

1.6. Thesis structure

In this study, large eddy simulation (LES) model with OpenFOAM is performed to study the characteristics of PSJ. The compressible jets are investigated in both single-and-multi orifice.

In chapter 2, the validation of LES (Large Eddy Simulation) involves comparing the pressure time histories within the cylinder to previous experimental data conducted on a similar model geometry of the PSJA. The relationship between pressure and Mach number are linked, and the examination of the velocity field for a single orifice jet is also included in the analysis. The investigation and presentation of the specific characteristics of the velocity field of the single orifice jet provide a comprehensive understanding of its behavior. Chapter 3 introduces the models featuring multiple orifices. The interaction of high-speed jets issued from a PSJA with multiple orifices is investigated with LES. The phase-averaged statistics are used to examine the interaction of the synthetic jets. The conclusion is summarized in chapter 4. The future works are introduced in chapter 5.

CHAPTER 2. A SINGLE SYNTHETIC JET

2.1. Piston-driven synthetic jet

Recently, some investigations of the fundamental characteristics of PSJAs were conducted on several experiments. These studies indicate that various independent parameters related to their geometry influences the performance of PSJAs, which must be determined during the design process. Traub et al. [63] did a test and concluded that a PSJA actuator with various piston frequencies and slot sizes. The result revealed that the jet velocity increase linearly with frequency. The cylinder size, piston stroke length and frequency, and orifice hole dimensions strongly affect the jet velocity. Investigation for conventional SJAs show similar influences [64]. However, for distinct geometries, building multiple test models of PSJAs can be costly, limiting the amount of information obtained from experimental work. In addition, experiments can only provide limited insights into distributions of velocity, pressure, and temperature. In contrast, numerical simulations have the potential to offer a wide range of information. Nevertheless, to study the flow induced by PSJAs, only some previous studies have utilized numerical simulations.

In this study, large-eddy simulations (hereinafter referred to as “LESs”) is utilized to analyze PSJAs [65]. Based on experiments of Sakakibara et al. [53], the numerical PSJA model is developed. Since the experimental apparatus has been successfully constructed in our laboratory, the pressure with the cylinder, a crucial parameter of PSJAs, is validated the numerical simulation with the experimental results. Previous experiments have demonstrated a relationship between the maximum jet Mach number and the maximum pressure inside the cylinder, which is also confirmed

through the simulation, also. Subsequently, the jet flow generated by PSJAs is investigated, an aspect not thoroughly explored in previous experimental studies.

2.2. Numerical Methods

2.2.1. PSJA Model

In the research, the simplified PSJA investigated is presented in Figure 2.1. The square shapes make use of the piston and cylinder to maintain simplicity, despite that in the experiment, it is a round-shape. Nonetheless, the compression ratio and actuator's size align closely with the experimental setup, enabling meaningful comparisons between experiments and numerical simulations. A d = 3 mm sidelength of square orifice is featured by the actuator. At the time the piston going to the bottom dead center (hereinafter referred as BDC), as depicted in Fig. 2.1, the cylinder length measures L = 21.7 mm. The stroke length is set to L_0 = 20.6 mm in order to ensure consistency with the experimental devices, matching the experimental values. The distance from the cylinder's top to the top dead center (hereinafter referred as TDC) is 1.1 mm. The point labeled P represents where temperature and pressure time series are recorded. Between midway the orifice's center and the cylinder's edge, on the cylinder's top surface, point P is located. The selection here is based on the experimental setup of PSJA [53]. On the cylinder's top wall, the pressure is measure as the pressure transducer is set up near the orifice. A cosine function describes the motion of the piston, which will be further explained when discussing the boundary conditions. The numerical parameter, the piston movement's frequency, denoted as f, remains constant.

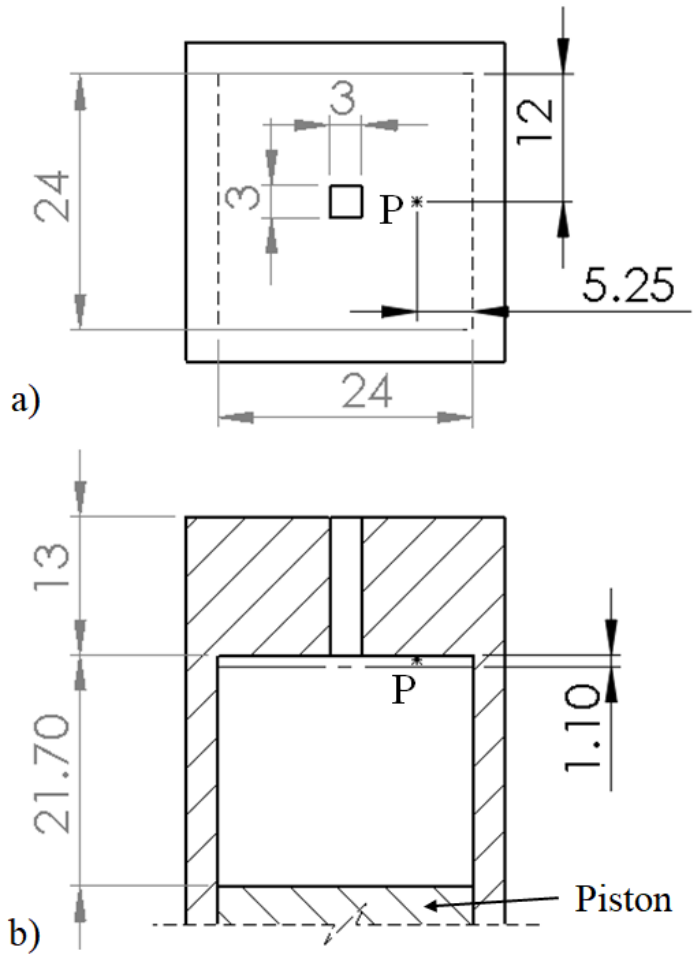

Figure 2.1. a) top view and b) cross-sectional frontal view of a synthetic jet actuator driven by a pistons (all lengths in millimeters).

2.2.2. Computational Approach

The governing equations are compressible Navier—Stokes equations, assuming an ideal gas is the working fluid. Besides, the LES solves the low-pass-filtered conservation equations of mass, momentum, and energy, which are expressed as follows [66]:

$$\frac{\partial \bar{\rho}}{\partial t} + \frac{\partial \bar{\rho}\tilde{u}_j}{x_j} = 0 \tag{2.1}$$

$$\frac{\partial \bar{\rho}\tilde{u}_i}{\partial t} + \frac{\partial \bar{\rho}\tilde{u}_i\tilde{u}_j}{\partial x_j} = -\frac{\partial \bar{p}}{\partial x_i} + \frac{\partial}{\partial x_j}\left(\bar{\tau}_{ij} - \tau_{ij}^{sgs}\right) \tag{2.2}$$

$$\frac{\partial \bar{\rho}\tilde{E}}{\partial t} + \frac{\partial}{\partial x_j}\left[\left(\bar{\rho}\,\tilde{E} + p\right)\tilde{u}_j\right] = \frac{\partial}{\partial x_j}\left(\alpha\frac{\partial \tilde{T}}{\partial x_j} - \tilde{u}_j\bar{\tau}_{ij} - H^{sgs} - \sigma^{sgs}\right) \tag{2.3}$$

with the equation of state for the ideal gas $\bar{p} = \bar{\rho}R\tilde{T}$. Here, $\bar{*}$ and $\tilde{*}$ are filtered and density-weighted filtered variables, respectively. $\bar{\rho}$ and $\bar{p}$ are the filtered density and pressure, respectively, $\tilde{u}_j$ (j = 1, 2, 3) is the filtered velocity vector, $\bar{\tau}_{ij}$ is the filtered shear stress tensor, τ^{sgs} is the sub-grid shear stress tensor ($\tau_{ij}^{sgs} = \bar{\rho}(\widetilde{u_i u_j} - \tilde{u}_i\tilde{u}_j)$). $\tilde{E}$ is the filtered total energy, $\tilde{T}$ is the filtered temperature, α is the thermal diffusivity, H^{sgs} is the sub-grid enthalpy flux, and σ^{sgs} is the sub-grid viscous stress tensor ($\sigma_i^{sgs} = \widetilde{u_j\tau_{ij}} - \tilde{u}_j\bar{\tau}_{ij}$).

LES with the Smagorinsky model is employed in this study with a software package, namely OpenFOAM. To handle the inducing of supersonic flow and the significant compression or expansion of the fluid in the cylinder, the *rhoPimpleFoam* solver is utilized. The solver combines the Semi-Implicit Method for Pressure-Linked

Equations (SIMPLE) [67] and Pressure Implicit with Splitting of Operators (PISO) [68] algorithms. Detailed explanations of the solver can be found in Holzmann [69]. For time discretization, the simulation utilizes the *backward* time scheme, a second-order accuracy of implicit method. Using the *Gauss linear* scheme combining Gauss' theorem and the second-order accurate central difference scheme is for spatial discretization. The time step size satisfies the Courant criterion, ensuring the Courant number is smaller than 0.5 for all cases.

2.2.3. Boundary Conditions and Domain Specification

The computational domain utilized in the simulations is depicted in Figure 2.2 a, consisting of three distinct regions: the outflow, the orifice, and the piston/cylinder domains. From the orifice, the jet is generated. In addition, all of these domains have rectangular shapes, with dimensions (*Lx, Ly, Lz*) provided in Table 2.1. The orifice outlet center is set as the origin (*x, y, z*) of the coordinate system.

Using the *blockMesh* utility, the mesh is generated. The method employs a non-uniform grid spacing for orthogonal grid. In the cylinder, to account for the piston's motion, in the *x*-direction, the cell size varies over time. In the outflow domain, a non-uniform grid spacing is implemented to enhance spatial resolution within the jet. As a result, in the outflow domain where is near the lateral and top boundaries, the cell size becomes larger. In the lateral direction, the minimum cell size is set at 0.5 mm, specifically adapted to the PSJA's centerline. Beyond that, as moving away from the center, by a ratio of 1.05, the lateral cell size increases. In the directions of *y* and *z*, to calculate the cell sizes, the same procedure is followed. Consequently, an illustration the computational domain's slice in Figure 2.2 b, in the streamwise direction, the cell size also expands from $x = 0$. The number of cells is decided based on the geometrical dimensions and the aforementioned approach provided in Table 2.1. Figure 2.2 c visualizes the region of interest with the grid distribution forming the jet flow.

The upper surface of the piston serves as the bottom wall of the cylinder section. As a result, the location of the cell size and the bottom boundary within the cylinder section undergo temporal variations. This functionality is implemented using

the *dynamicInkJetFvMesh* class in OpenFOAM. During each cycle, the piston velocity reaches its maximum absolute values at the midpoint of the stroke length and gradually approaches zero at the TDC and BDC. The piston/cylinder domain changes as the result of the piston movement. Based on the piston position, the mesh distribution is adapted accordingly, while the cell number remains constant throughout the calculations. Figure 2.3 a illustrates, when the piston positioned at either the TDC and BDC, the mesh is distributed. By a cosine function, the position of the piston, denoted as x_P, is determined explicitly

$$x_p = x_c + \frac{1}{2} L\cos(2\pi f t + \omega_0), \tag{2.4}$$

where t representing the time and initial phase $\omega_0 = \pi$, the piston movement's central position is denoted as $x_c =$ -24.4 mm. This value ensures that the piston is in the lowest position with zero velocity. By taking derivative of x_P by time, Figure 2.3 b displays time variation of the velocity of piston Up in one cycle $T = 1/f$.

All computational boundaries are subject to the *waveTransmissive* boundary condition in the outflow domain (as shown in Figure 2.2 a), exclude for the surface containing the orifice. This works as a non-reflecting boundary condition. As the region of interest involves the boundary layers on these surfaces and the outflow from the orifice are not the focus of observation, the interior surface of the cylinder and surface of the orifice is applied by the slip condition. The piston's top surface is treated as a boundary that moves with a velocity determined by Eq. (2.4). The implementation of this boundary condition by using the *movingWallVelocity* class is built into the OpenFOAM code.

The entire domain employs the same initial conditions. All three components of the velocity vectors is set to zero as the initial velocity. The temperature, T_0, is set to 300 K. The atmospheric pressure is used as initial pressure, P_{atm} = 101,325 Pa. This study conducts simulations for frequencies f from 50 to150 Hz, with increment of 25 Hz. In each case, the simulation is advanced over a time span of 6T. The simulation is extended to 20T to calculate the velocity statistics of the jet when f = 100 Hz. To eliminate transient behavior resulting from the initial state, the results are obtained after the fourth cycle.

Table 2.1. The cell numbers and size of domains

Domain	Number of cells (Nx, Ny, Nz)	Size (mm) (Lx, Ly, Lz)
Piston/Cylinder	(24, 36, 36)	(21.7, 24, 24)
Orifice	(26, 6, 6)	(13, 3, 3)
Outflow domain	(74, 138, 138)	(360, 483, 483)

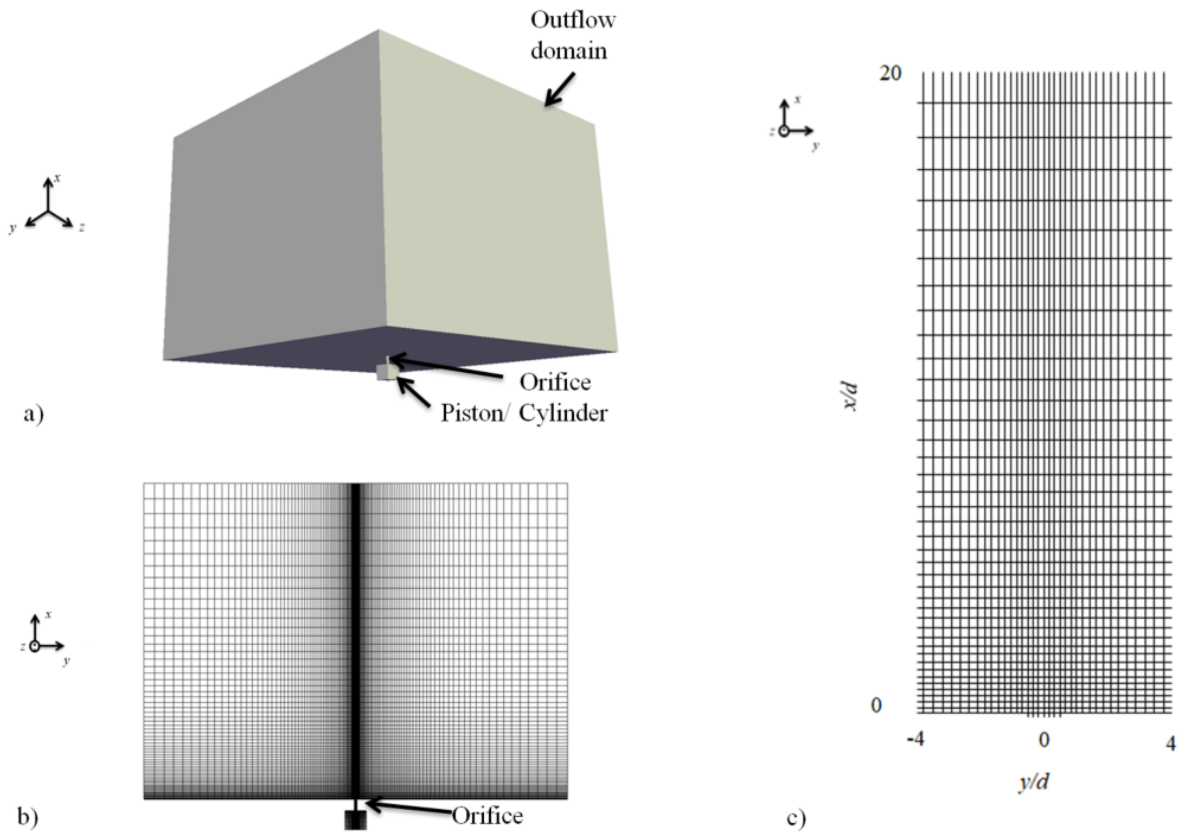

Figure 2.2. The grid and computational domain: a) the whole domain; b) cross-section; c) the grid in $-4 < y/d < 4$ and $0 < x/d < 20$.

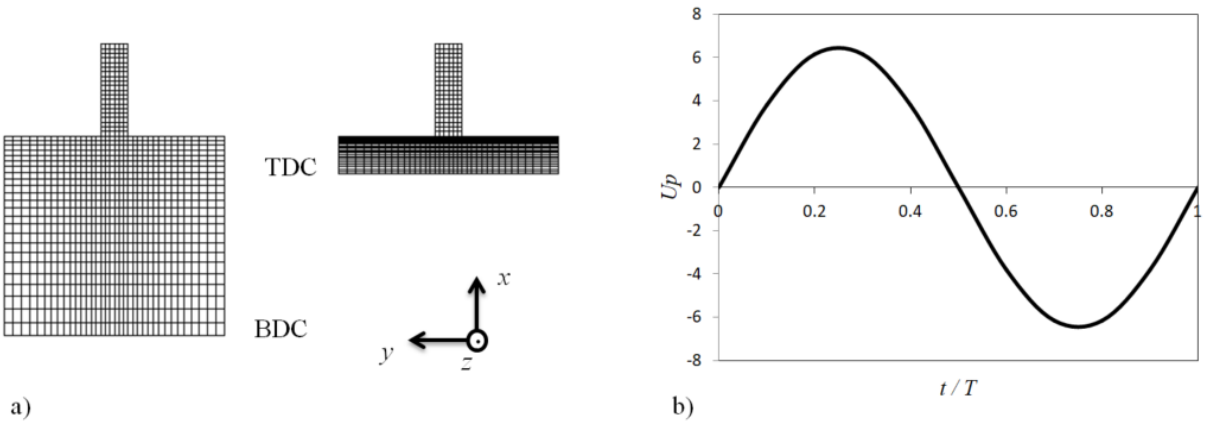

Figure 2.3. a) Grid movement from BDC to TDC and b) piston velocity in one cycle.

2.2.4. Grid independence test

The simulation case of 100 Hz undergoes a grid independence test, wherein a smaller number of cells is employed in an additional simulation, as presented in Table 2.2.

Table 2.2. In the test case, the variation of sizes of domain and the cell numbers.

Domain	Number of cells *(Nx, Ny, Nz)*	Size (mm) *(Lx, Ly, Lz)*
Piston/Cylinder	(15, 21, 21)	(21.7, 24, 24)
Orifice	(13, 3, 3)	(13, 3, 3)
Outflow domain	(60, 111, 111)	(360, 483, 483)

Figure 2.4 compares the time-based pressure profiles at point P inside the cylinder. By the period *T,* time *t* is normalized and by absolute pressure P_{atm}, P_r is also normalized ($P_r = \bar{p}/P_{atm}$). By piston motion, the pressure is affected by the working fluid's expansion and compression. This effect is also associated with the jet velocity at location of the orifice exit, as discussed in the next section. As the normalized pressure P_r is smaller than 1 and larger than 1 in the suction and blowing phase, respectively, the pressure profiles are influenced by the intermittent behavior of the PSJ. The outcomes reveal minimal dissimilarity between the two cases with varying resolutions, indicating that the resolution does not affect the behavior of the jet.

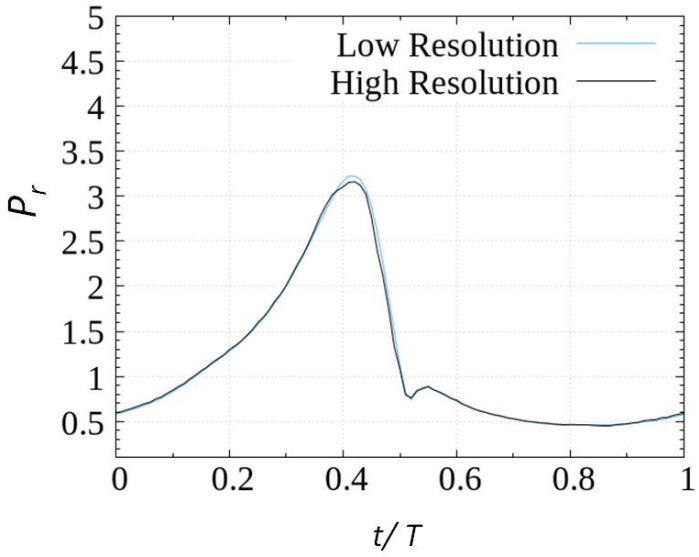

Figure 2.4. For f = 100 Hz in two cases of resolutions, the normalized pressure P_r is compared.

2.3. Results and Discussions

2.3.1. The pressure profiles over time

Within the cylinder, the pressure is associated with the jet velocity [53]. On the cylinder's inner surface at point P, time-series data of pressure is collected. Figure 2.5 compares the normalized absolute pressure ($P_r = \overline{p}/P_{atm}$) during two cycles at frequencies of 50 Hz, 75 Hz, 100 Hz, and 150 Hz. As the piston is positioned at the BDC, the pressure between the two cycles is minor.

Figure 2.6 depicts the frequency dependency of P_r. A higher frequency leads to delayed attainment of peak pressure in terms of time (t_{peak}/T). For frequencies of 50, 75, 100, and 150 Hz, the values of t_{peak}/T are 0.345, 0.383, 0.410, and 0.433, respectively. As the frequency increases, when the piston resides at the TDC, these values shift closer to the time t/T = 0.5. The pressure profiles exhibit noticeable asymmetry, as also reported in experimental observations [53]. The asymmetric pressure variation occurs due to the compressibility effect (the density variation). As the piston moves upward, the pressure increases in the cylinder, and at the same time, the density varies. Also, when the piston moves up, the volume remaining in the cylinder becomes small and the pressure increases toward the maximum pressure. The process then, as the piston continues to move up the TDC, causes the pressure to decrease because of the ejection of fluid through the orifice. When the flow outside entering the cylinder causes the pressure to fall rapidly, i.e., $\partial P/\partial t$ increases quickly because of the moving down of the piston in the suction phase. When considering a cycle, the maximum pressure point is smaller than $0.5T$, which makes the time for the suction phase to be larger than $0.5T$. Logically, the $\partial P/\partial t$ in the suction phase should

be larger than the blowing phase. When the frequency is small, for example, f = 25 Hz, the compressibility effect is negligible because of a tiny variation of the cylinder pressure to the atmosphere pressure. For this case, the low-frequency piston synthetic jet is treated as a conventional synthetic jet [34] [17], so the pressure profile remains almost symmetric [53]. Generating a nearly symmetric pressure profile also implies a nearly symmetric rise and fall of the flow through the orifice. Derived from the symmetric motion of the piston, the piston velocity is derived by the position function, which is also symmetric. Hence, the direct relation to the inflow and outflow through the orifice is also almost symmetric. In other words, the compressibility effect causes the maximum pressure to take place before 0.5T, resulting in an asymmetric pressure profile. The increase in pressure is only possible when the fluid is incompressible.

Figure 2.7 presents the pressure histories between the experimental and for the case of diameter d = 3 mm [53], by a single-round orifice, simulation outcomes of the PSJA is compared. Despite the dissimilarity in orifice shapes between the experiment and simulation, their compression ratio (S_1/S_2) between the cylinder's the cross-sections (S_1) and the orifice (S_2) remain unchanged. To facilitate comparison with experiments where piston position was not measured, the results are plotted against (t - t_{peak})/T. Within this figure, the pressure histories with frequencies of 50, 75, and 100 Hz are compared for both simulations and experiments. In contrast, for f = 150 Hz, simulation data is provided, as a reference. The maximum pressures rises while the minimum pressure falls as the frequency increases. Notably, the pressure histories exhibit agreement between the experiments and simulations, despite the utilization of different orifice shapes. This similarity comes from the same compression ratios between the two cases, as mentioned above. However, with different orifice shapes,

the velocity outside the orifice exit can differ, resulting in different heat transfer between these two orifice shapes [70].

The maximum and minimum normalized pressures, P_{rmax} and P_{rmin}, are depicted in Figure 2.8, and their comparison with the experimental data [53] is presented. The frequency dependency of both P_{rmax} and P_{rmin} exhibits close correspondence with the empirical findings. When $P_r \geq 1.893$ during the blowing phase and $P_r \leq 0.528$ during the suction phase, inside the orifice hole, the flow is anticipated to become sonic [53]. Horizontal dashed lines indicate these conditions. The outcomes of the experiments and simulations indicate that for frequencies greater than 100 Hz, both conditions are met. Nonetheless, when the frequency surpasses approximately 60 Hz, in the blowing phase, the flow can reach sonic requirements.

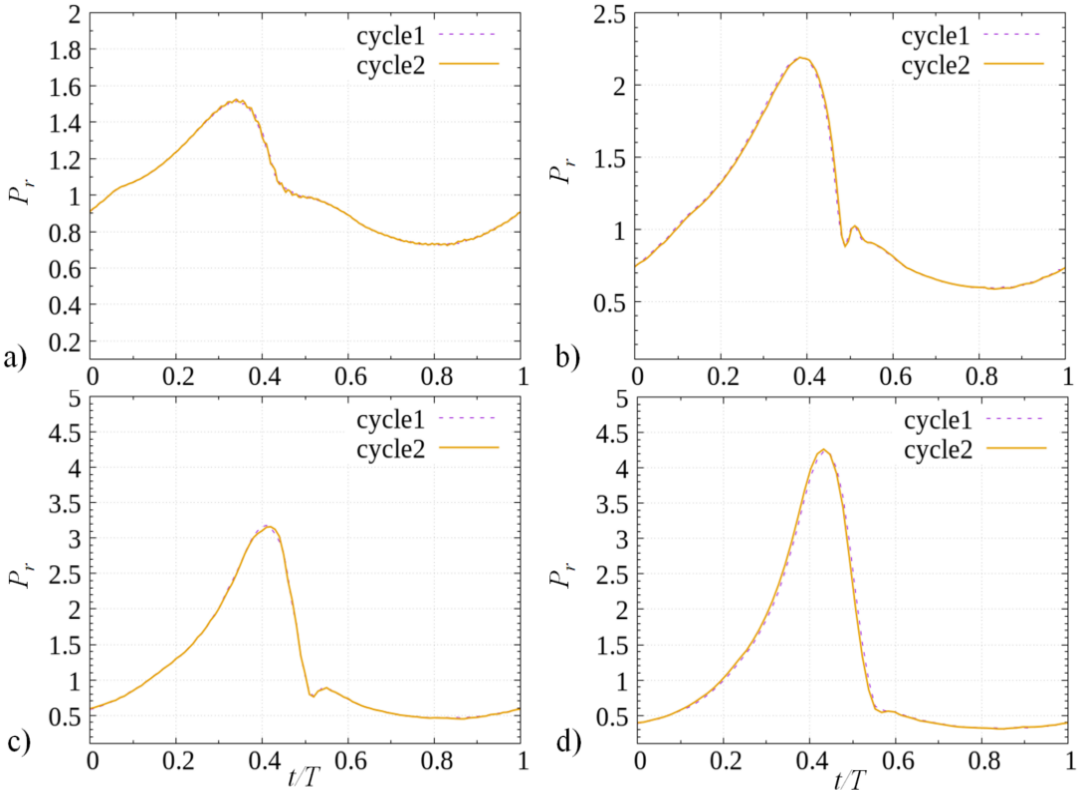

Figure 2.5. The normalized pressure P_r for different frequencies a) f = 50 Hz, b) f = 75 Hz, c) f = 100 Hz and d) f = 150 Hz.

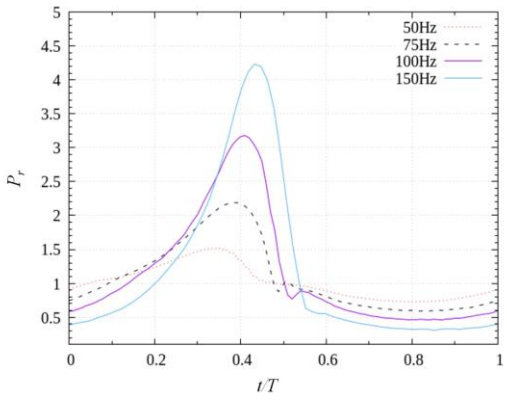

Figure 2.6. Normalized pressure in time series.

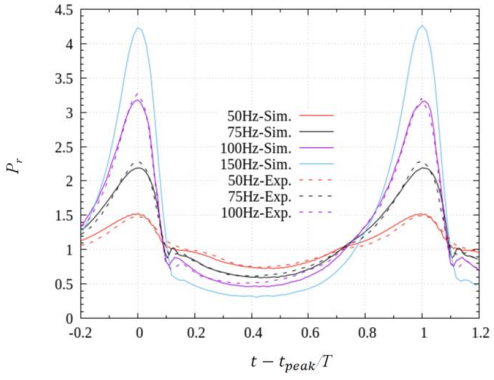

Figure 2.7. Normalized pressure of simulation (Sim.) is compared with the experiment (Exp.).

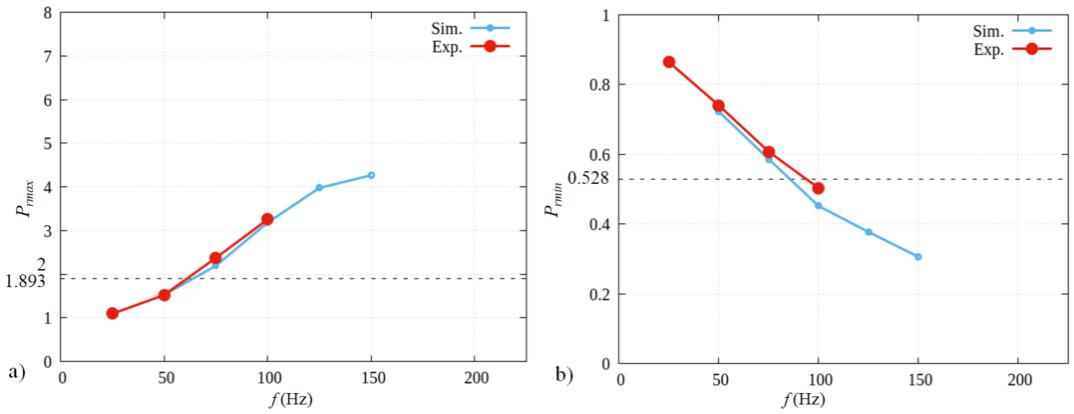

Figure 2.8. Dependence of a) maximum and b) minimum normalized pressures.

2.3.2. History of Mach Numbers

Figure 2.9 represents the Mach number at the orifice outlet, $M = |\tilde{\boldsymbol{u}}|/a$. Here, at the orifice exit, $\tilde{\boldsymbol{u}}$ is the velocity vector, a is the local sound speed. With the change of flow directions between suction and blowing phases, the Mach number is toward zero, and then attains a local minimum. It is possible to identify this approximately as time with t/T smaller than 0.5, and time with t/T larger than 0.5. In the directions of y and z, this could be affected by the non-zero velocity. At t/T= 0.25 as the piston reaches its highest velocity, in the midpoint of the semi-cycle, the maximum value is not reached. The time is delayed with the increasing frequencies. Figure 2.5 has shown, in the cylinder, the tendency between the maximum pressure and the time. As the pressure reaches the maximum, the maximum Mach numbers are close to times at which. In details, for f = 50 Hz, the time achieved at t/T = 0.340; for f = 150 Hz, the time achieved at t/T = 0.429 (f = 75, 100 Hz, the time t/T = 0.383, 0.430, respectively). In the case of frequency values of f = 50 Hz, 75 Hz, 100 Hz, and 150 Hz, the first minimum value of M, M_{min}, also rises during the cycle: t/T reaches respectively at 0.06, 0.11, 0.15, and 0.21. Figure 2.6 indicates that when P_r = 1, these times approximately corresponds. These results suggest the strong relation between P_r and M. The Mach number declines dramatically, as soon as it reaches its maximum, also same as P_r tendency.

For an isentropic flow through a Laval nozzle, the value of the Mach number, M_{is}, is calculated [71]:

$$\frac{p_0}{p} = \left(1 + \frac{\gamma-1}{2} M_{is}^2\right)^{\frac{\gamma}{\gamma-1}}, \tag{2.5}$$

where p denotes the pressure at M_{is}, p_0 represents the stagnation pressure, the specific heat ratio γ is 1.4. Based on Eq. (2.5), we anticipate the subsequent correlation between M_{max} and P_{rmax}:

$$M_{max} = \left\{ \frac{2}{\gamma - 1} \left(P_{rmax}^{\frac{\gamma - 1}{\gamma}} - 1 \right) \right\}^{\frac{1}{2}}, \tag{2.6}$$

Figure 2.10 illustrates the variation of M_{max} in relation to P_{rmax}. As anticipated, an increase in P_{rmax} corresponds to a higher M_{max}. The simulation results closely align with the theoretical predictions, and based on the pressure within the cylinder, Eq. (2.6) is proved to be valuable in evaluating the maximum Mach number. Nonetheless, experimental findings [53] indicate a slight deviation from Eq. (2.6), suggesting that the experimental Mach number is a bit lower. This disparity can be attributed to the inclusion of viscous effects within the orifice due to the application of the slip boundary condition. Additionally, according to the theory of isentropic flow, as the piston ascends, gradually increasing the pressure, the outflow region is perceived as an expanded area. Consequently, when the pressure decreases, the velocity of the jet flow rises proportionately.

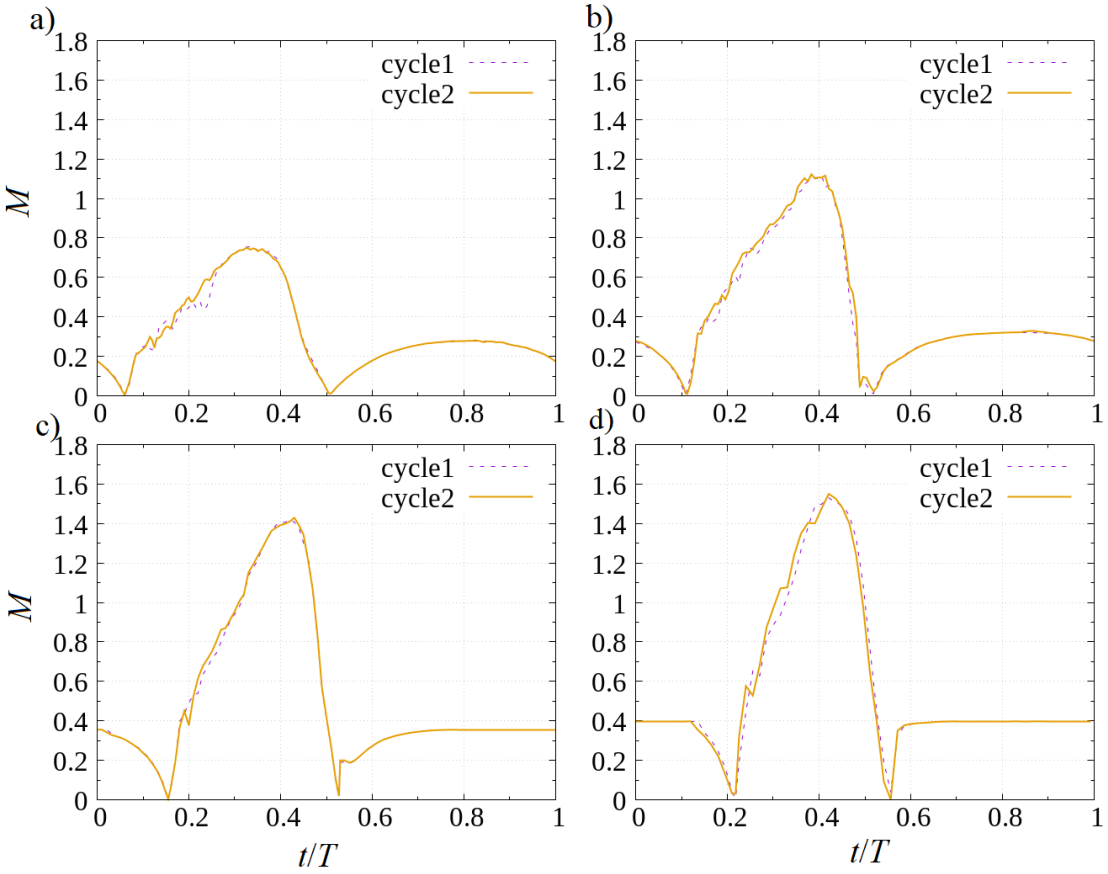

Figure 2.9. For various frequencies, Mach number is plotted in time series (the frequency and order are same as in Figure 2.5).

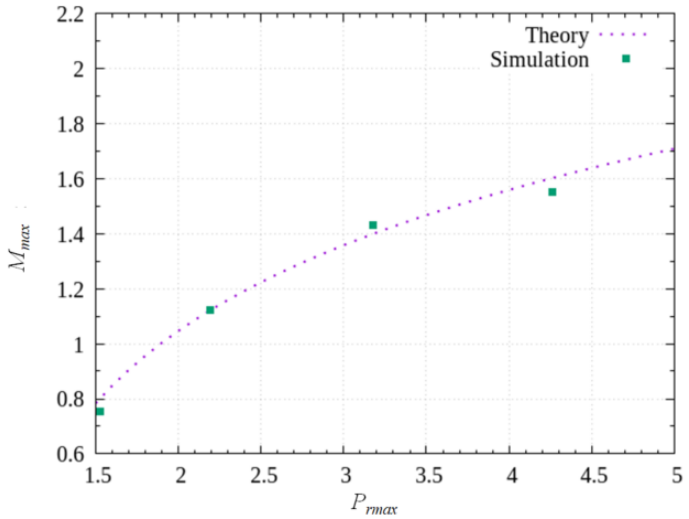

Figure 2.10. The maximum Mach number and pressure.

2.3.3. Temporal evolutions of temperature within the cylinder

Within the cylinder at point P (the position P in Figure 2.5, Figure 2.6, and Figure 2.7), the time evolutions of temperature are illustrated in Figure 2.11. In this figure, $T_r = \tilde{T}/T_0$ is the normalized temperature $\tilde{T}$ with respect to the ambient temperature T_0, is displayed. The temperature trend closely mirrors that of pressure due to the strong coupling between variations in pressure and gas temperature governed by equation of state mentioned in section 2.2.2 about Computational Approach . The time interval between the phases of blowing and ingesting of the piston's movement is relatively shorter, which may contribute to this more pronounced variation. These findings are qualitatively agreed with the simulation conducted by Crittenden et al. [34], wherein an increase in frequency leads to an elevation in gas temperature. For frequencies of 50, 75, 100, and 150 Hz, the maximum temperature values are observed as 364, 425, 592, and 802 K, respectively. The case of reaching 800 K of 150 Hz is the case that matches the maximum of the above results. It also corresponds to maximum cylinder pressure. Because heat transfer is proportional to differences between the temperature near the wall and wall temperature, in the case of 150 Hz, the maximum temperature is higher than in other cases. In comparison, the minimum temperature is lower than others. The differences lead to it has the largest heat transfers in both suction and blowing phases. This temperature rise within the cylinder holds significance in the PSJA’s experimental study. Using tracer particles seeded with engine oil evaporated due to temperature variations within the cylinder to study turbulence generated by the PSJAs, Yamamoto et al. [55] conducted a velocity measurement technique.

The present results suggest that at high frequencies, the seeding method necessitates substantial temperature variations in case of temperature-dependent luminescence properties.

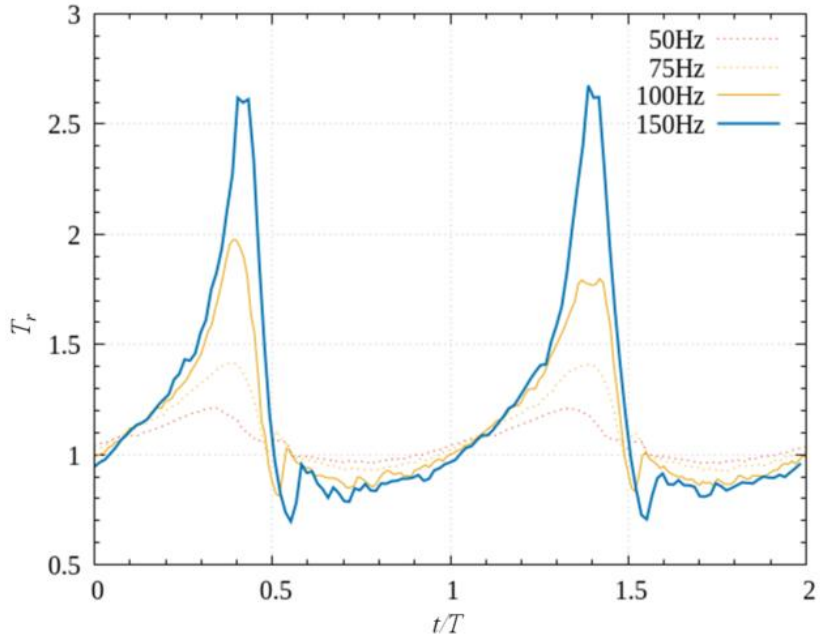

Figure 2.11. The temperature profiles within the cylinder over time are examined for varying frequencies.

2.3.4. Reynolds Number History

At the orifice exit for various frequencies, Figure 2.12 presents the variations of the Reynolds number (*Re*). In this context, *Re* is characterized by

$$Re = \frac{\bar{\rho}|\tilde{\boldsymbol{u}}|d}{\bar{\mu}}, \tag{2.7}$$

where $\bar{\mu}$ corresponds to the viscosity coefficient, d signifies the sidelength of the orifice, $|\tilde{\boldsymbol{u}}|$ denotes the velocity at position of the orifice outlet and $\bar{\rho}$ represents the density. At (y, z) = (0, 0), *Re* is assessed. Even in the case with the lowest frequency, *Re* exceeds 50000 in the blowing phase. Consequently, the jet emitted from the orifice undergoes a transition to turbulence. Within one cycle, the highest *Re* exhibits an increase with the frequency *f*. Specifically, for frequencies of 50, 75, 100, and 150 Hz, the corresponding maximum *Re* values are 4.9×10^5, 7×10^5, 8.3×10^5, and 8.4×10^5. During the flowing phases, the times at which these maximum values are reached coincide with the changes in pressure as depicted in Figure 2.6. The rate of increase of the maximum Re becomes slower as the frequency *f* rises, aligning with the frequency dependence observed for the maximum Mach number in Figure 2.9. Consequently, when the frequency *f* is sufficiently high, the jet behavior exhibits a diminished dependence on *f*.

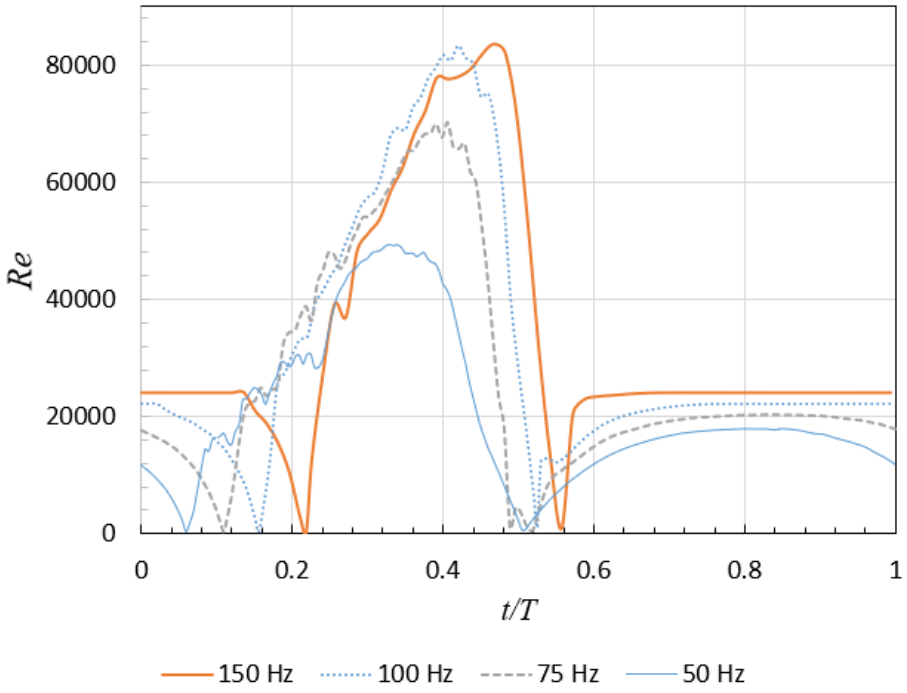

Figure 2.12. Temporal profiles of Reynolds numbers are examined for various frequencies.

2.3.5. Phase-averaged Flow-field

Through the orifice hole, the periodical jet is discharged. Consequently, by using a phase average, an examination of the velocity flow field within the jet is conducted. The time can directly correlate with through Eq. (1), in which piston position x_p is conditioned. In the x-direction, the color contour representing the phase-averaged velocity, denoted as U, where Figure 2.13 presents the flow field is within the jet, for a frequency of 100 Hz. Additionally, Figure 2.14 depicts the variation of U along the centerline of the jet, with beginning of the orifice hole. The progression of time ranging from (a) to (j) in increments of $0.1T$ is showcased by these figures.

Despite the movement towards the TDC of the piston, the flow corresponds to the suction phase, where the direction of flow is towards the cylinder ($U < 0$) at t/T = 0.1 (Figure 2.13 a and Figure 2.14 a). However, by t/T = 0.2 (Figure 2.13 b and Figure 2.14 b), there is a significant change in the velocity profile, and the jet is forcefully expelled outward via the orifice. The x-direction velocity decelerates in the region nearly x/d = 4-6, implying that the jet has arrived this region, at t/T = 0.2. Subsequently, when around t/T = 0.4, with the maximum velocity reaching the orifice outlet, the jet velocity experiences a substantial increase (Figure 2.13 d and Figure 2.14 d). Next to this, the velocity steadily decreases and transitions into the phase of ingesting. In the same time, the velocity towards the orifice is noticed near the orifice outlet. Nonetheless, in Figure 2.14 (f-j), during the suction phase, the flow-induced effects have limited reach beyond the orifice: for $x/d > 2$, U approaches 0. Using particle image velocimetry, the results obtained exhibit qualitative agreement with the experiment conducted, ranging from $0.3T$ to $0.5T$ [34]. As the jet velocity increases,

the study reported the appearance of shock cells with the inner jet in the vicinity of the orifice.

Although the large-eddy simulations fail to accurately capture the shock structures due to limited spatial resolution, the presence of velocity oscillations during the region of $0 < x/d < 2$, which is around the jet outlet confirms the occurrence of shock cells.

Figure 2.15 illustrates, in the streamwise direction, root-mean-square (hereinafter referred as rms) of the velocity fluctuations at specific phases, denoted as u_{rms}, along the centerline from the orifice. The time interval ranges with a growth of $0.1T$ from $t/T = 0.1$ to 1. The calculation of u_{rms} is based on twenty consecutive snapshots of piston cycles using the phase average. From Figure 2.15, from $t/T = 0.2$ to 0.4, during the period (b-d), it is observed that high levels of turbulence occurs. At $t/T = 0.2$, as shown in Figure 2.14 b, the velocity fluctuations are significant, and the jet tip experiences strong turbulent fluctuations when the jet reaches x/d = 4-6. Notably, turbulence levels are especially high at far positions from the orifice, specifically at $t/T = 0.3$ and 0.4 in the range $x/d > 10$, respectively. In Figure 2.15 e, when the piston reaches the position of TDC, in the near field, u_{rms} also reaches a peak at $t/T = 0.5$. This period aligns with the substantial decrease in P_r, as depicted in Figure 2.6. Consequently, at this time the high u_{rms} observed in the near field, which may be attributed to the significance of the jet deceleration. In the suction phase (Figure 2.15 (f-j)), the turbulence level is considerably lower compared to the blowing phase. With significant values occurring off the jet centerline, by both the velocity fluctuations u_{rms} and the gradient of mean velocity, velocity fluctuations in a turbulent

jet are generated [72] [41]. As observed in Figure 2.13 (b-d), the substantial transverse gradient of of $\widetilde{U}$, $\partial\widetilde{U}/\partial z$ ($\partial\widetilde{U}/\partial y$ owning to the symmetry, also), contributes to the generation of significant velocity fluctuations during the blowing phase. Nevertheless, in the phase of ingesting, the gradient of mean velocity is slight shown in Figure 2.13 (f-j), leading to minimal turbulence. Figure 2.16 shows the v_{rms} and w_{rms} at 0.4 T for the blowing phase and 0.8t for the suction phase. Because of jet's symmetry, the v_{rms} and w_{rms} values at each time point are quite similar. Also, at 0.4T, the v_{rms} and w_{rms} reached much higher values than 0.8T at the suction phase.

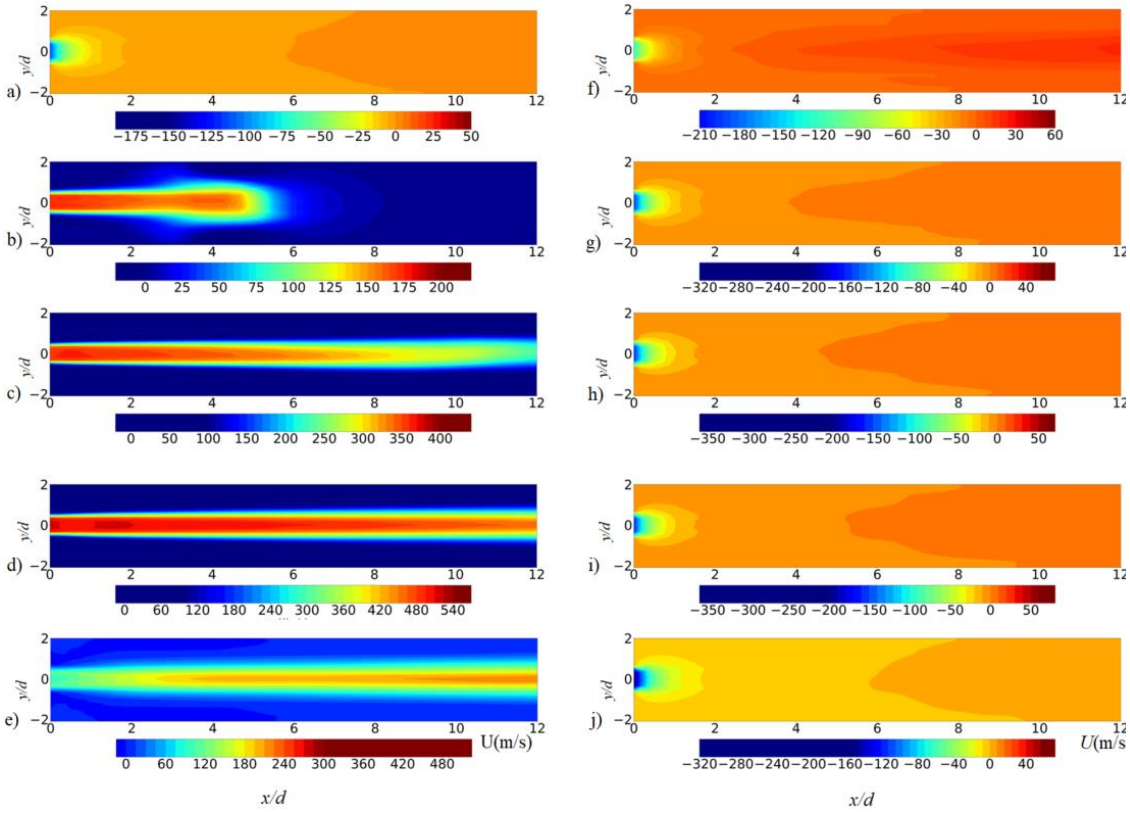

Figure 2.13. For f = 100 Hz with t/T from 0.1 to 1 by increment of 0.1 for a-j, phase-averaged velocity is visualized in the streamwise direction.

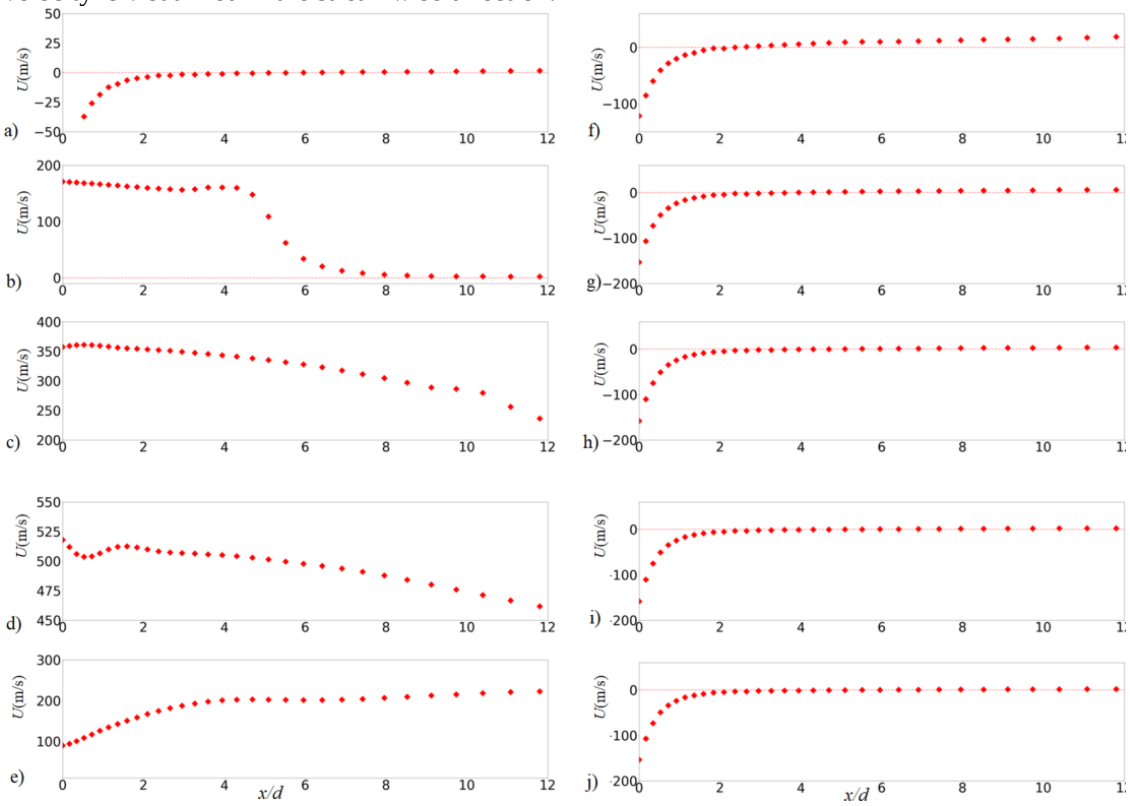

Figure 2.14. For a frequency of 100 Hz, the phase-averaged velocity of centerline is depicted at the following time instances with *t/T* from 0.1 to 1 by increment of 0.1 for a-j.

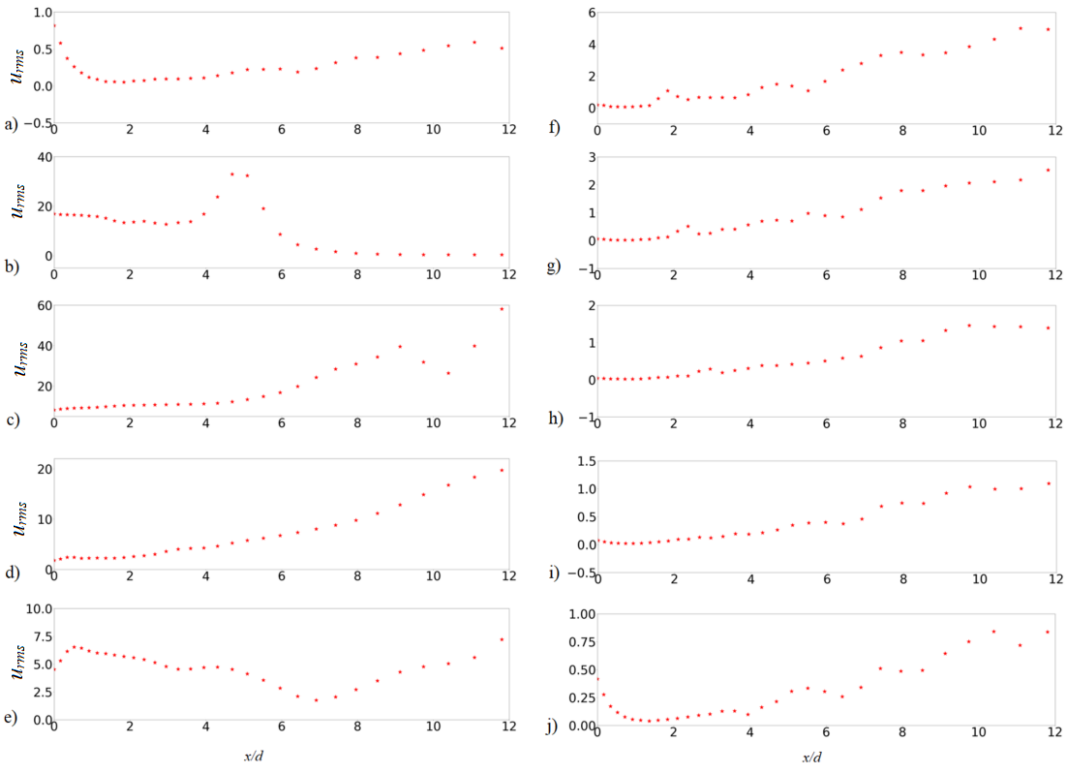

Figure 2.15. The root-mean-square (rms), u_{rms}, along the centerline of velocity in the streamwise direction for a frequency of 100 Hz at the following time instances with *t/T* from 0.1 to 1 by increment of 0.1 for a-j.

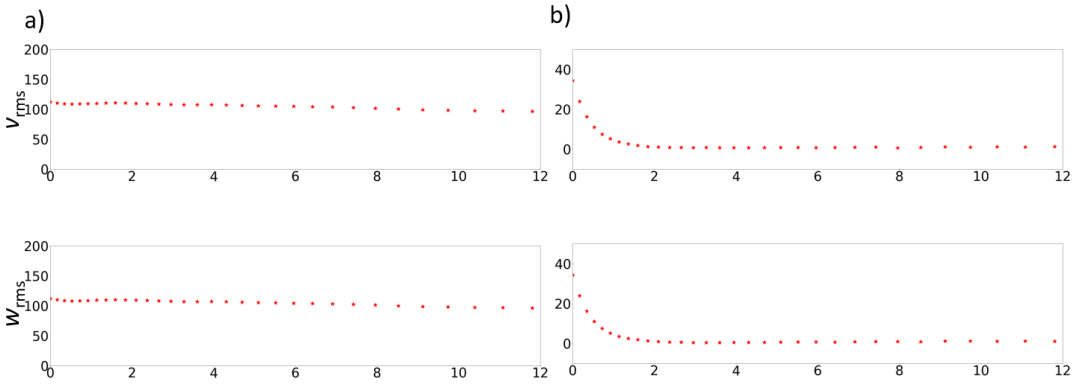

Figure 2.16. v_{rms} and w_{rms} at the same position as Figure 2.15 a) 0.4*T* b) 0.8*T*.

2.4. Concluding remarks

With a square orifice utilizing Large Eddy Simulations (LES) implemented in OpenFOAM, this study examined the compressible flow characteristics in which a PSJA produces the flow. The accuracy and reliability of the LES approach were validated through a comparison of the time-series data of pressure within the cylinder with experimental data obtained from previous studies conducted on a similarity of the geometric model of the PSJA. The results demonstrate that the numerical schemes utilized in this investigation are effective in analyzing the flow generated by PSJAs. For future studies, this capability will be crucial focusing on PSJAs with diverse geometries.

The Mach number at the orifice exit and the pressure within the cylinder exhibit minimal fluctuations across different cycles of piston movement, indicating statistically identical jet characteristics throughout. The maximum pressure increases while the minimum pressure decreases with higher frequencies *f*. The correlation between the highest pressure and Mach number aligns well, consistent with theoretical estimates. Additionally, the pressure variations within the cylinder lead to corresponding temperature fluctuations. Notably, at a piston frequency of 150 Hz, the highest temperature inside the cylinder surpasses 800 K. Concurrently, at the orifice outlet, the jet *Re* can attain an approximate value of 8.3×10^5, demonstrating an increase in Re with increasing frequency *f*. However, the frequency dependence weakens at higher frequencies.

Examination of the phase-averaged velocity field reveals that the phase of blowing does not perfectly align with the upward movements, and the suction phase

also does not completely match the downward motions of the piston. In the same manner, the timing of the maximum Mach number does not correspond with the maximum cylinder pressure's time. The rms, velocity fluctuations (u_{rms}) are significant in regions where the flow experiences deceleration at the furthest position from the jet. In the near field, the presence of large u_{rms} can be attributed to the substantial slowdown of the jet. Turbulence levels increase in the far field when the Mach number reaches its maximum value. In contrast, velocity fluctuations are relatively small during the suction phase owing to the reduced the gradient of mean velocity in the transverse direction of the jet.

CHAPTER 3. FLOW FIELD BY MULTI-SYNTHETIC JETS

3.1. Multi-orifice synthetic jets

This chapter reports numerical simulations of a multi-orifice PSJA. The performance of the simulated PSJA is tested by comparing the pressure variation in the actuator and the pressure dependence of the maximum jet Mach number with experimental data. Furthermore, the interaction of multiple synthetic jets is investigated with velocity statistics.

3.2. Numerical Procedures

3.2.1. Piston Synthetic Jet Model

Derived from the experimental study by Sakakibara et al. [53], the PSJA model is proposed. At the cylinder top with an orifice plate, the PSJA consists of a piston/cylinder actuator. We consider the PSJAs with two or four orifices, as shown in Figure 1. The basic dimensions also follow the experiment [53]. Here, we use square orifices instead of the round orifice to simplify the computational model, although synthetic jets often use the latter. Our previous study has confirmed that the performance of the PSJA is similar for square and round orifices as long as the orifice area is identical. For both two- and four-orifices models, the side dimension of square orifices is d = 2 mm. They are placed in symmetrical positions at a distance of 2 mm and in the center of the top wall of a square cylinder with a sidelength of 24 mm. The cylinder lengthss L = 21.7 mm, piston stroke of L_0 = 20.6 mm and the point P for sampling pressure are the same as the single orifice case in chapter 2.

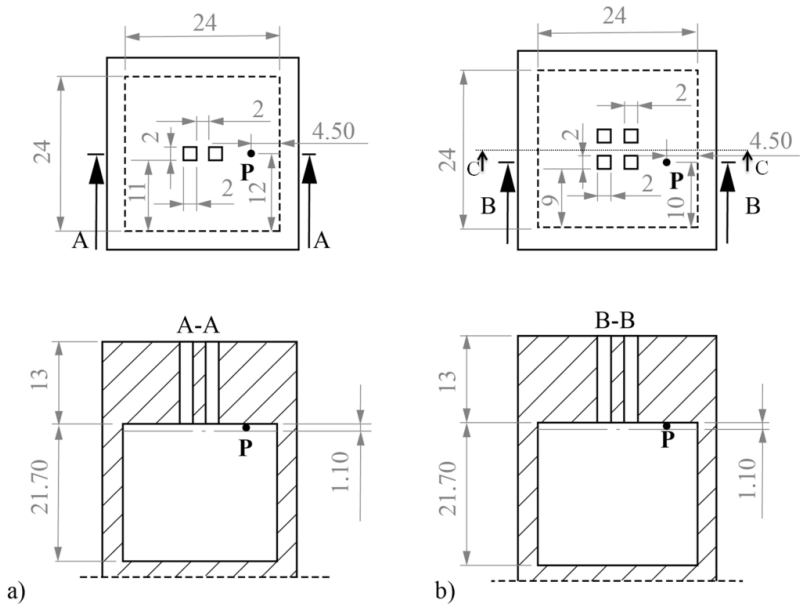

Figure 3.1. a) two-orifice model; b) four-orifice model of PSJA (all dimensions are in mm).

3.2.2. Computational Method

Similar to the domain of single-orifice jet, the computational domain consists of three parts: the piston/cylinder part for piston movement, the outflow part where the synthetic jet forms, and the orifice part which connects the other two parts, as shown in Figure 3.2 a. The orifice parts have two orifices or four orifices depending on the models. The rectangular blocks are used for these parts. With the two-orifice model, in Table 3.1, each part has a size of (*Lx, Ly, Lz*). The coordinate origin of this model is set at the center of two orifices. Similarly, with the four-orifice model, each part has its parameters listed in Table 3.2. At the four orifices outlet center, the coordinate origin is set. The noticeable points are the number of meshing blocks in the cylinder domain increasing as the number of orifices increasing in the orifice domain.

Large eddy simulation (LES) is performed with OpenFOAM. The numerical method is similar with a single orifice in the previous chapter. Figure 3.2 b shows a slice through the center of two orifices, and a part of the region of interest is shown in Figure 3.2 c, where the jets is generated.

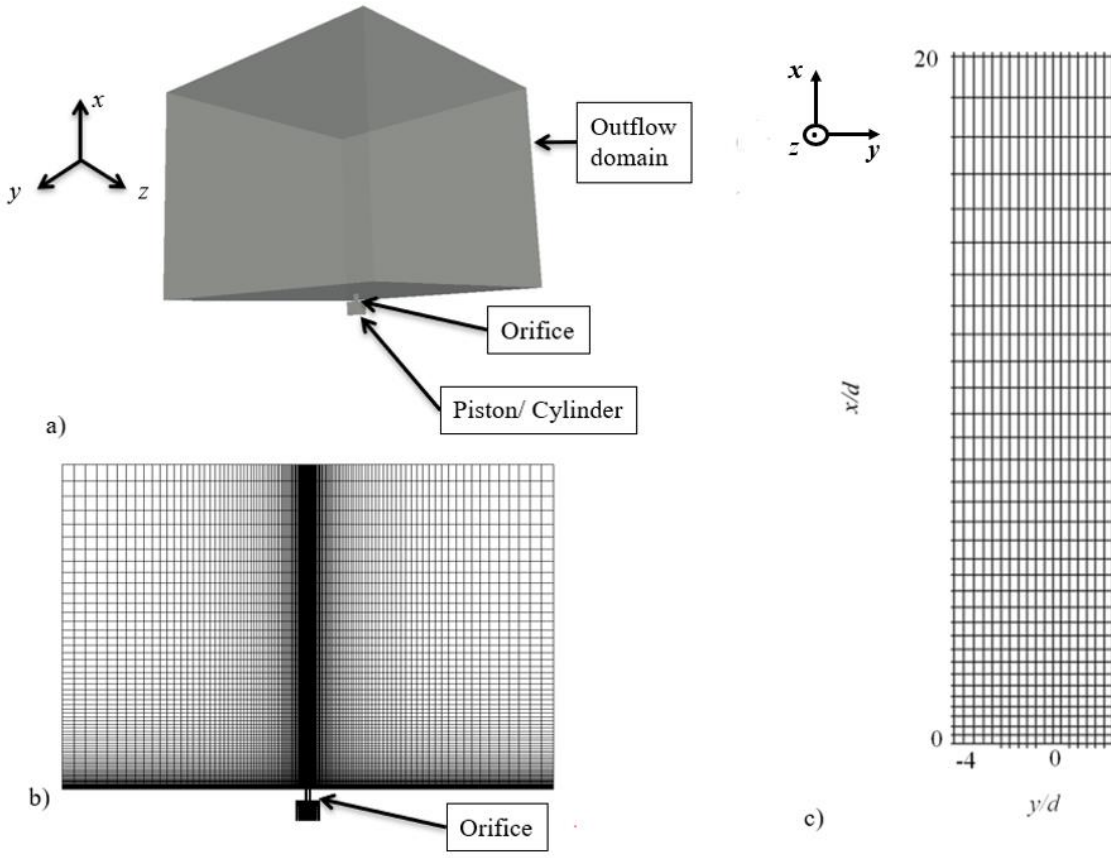

Figure 3.2. a) The whole domain; b) the center plane of grid distribution through two orifices; c) the grid distribution of the orifice area.

Table 3.1. The cell numbers and size of domains for the two-orifice model.

Domain	Number of cells (*Nx*, *Ny*, *Nz*)	Size (mm) (*Lx*, *Ly*, *Lz*)
Piston/Cylinder	(24, 38, 34)	(21.7, 24, 24)
Orifice	(26, 4, 4) ×2	(13, 2, 2) ×2
Outflow domain	(74, 144, 136)	(360, 486, 482)

Table 3.2. The cell numbers and size of domains for the four-orifice model.

Domain	Number of cells (*Nx*, *Ny*, *Nz*)	Size (mm) (*Lx*, *Ly*, *Lz*)
Piston/Cylinder	(24, 38, 38)	(21.7, 24, 24)
Orifice	(26, 4, 4) ×4	(13, 2, 2) ×4
Outflow domain	(74, 144, 144)	(360, 486, 486)

The piston movement method in Chapter 2 is employed. The initial conditions and other simulation conditions are set up the same as the single-orifice simulation.

3.3. Results

3.3.1. Pressure Histories

The pressure within the cylinder is a characteristic parameter having a relationship with the jet velocity [53]. Inside the cylinder, the pressure taken at point P (Figure 3.1) is compared with the measuremental results. The verification with the single orifice for different frequencies demonstrates a significant alignment between the simulation and experimental findings. For the two-orifice case at 100 Hz, we compare these pressure histories in Figure 4, which presents the normalized pressure P_r (explained in Chapter 2). Here, t/T = 0 and 1 indicate that the piston reaches at the BDC while t_{peak} is the time at which the maximum pressure is achieved. The simulation (Sim.) and experiment by Sakakibara et al. [53] agree well in terms of both peak and temporal variation. When comparing with experiments by Eri et al. [54] with the same frequency of 100 Hz, the difference is observed for the maximum pressure because of the differences in the volume displacement and the areas of the orifice exit. However, the overall shape of the pressure history is similar. Both numerical and experimental results exhibit a highly non-symmetric pressure variation, which is a signature of a high-speed synthetic jet. This comparison further validates the present numerical model of the PSJA.

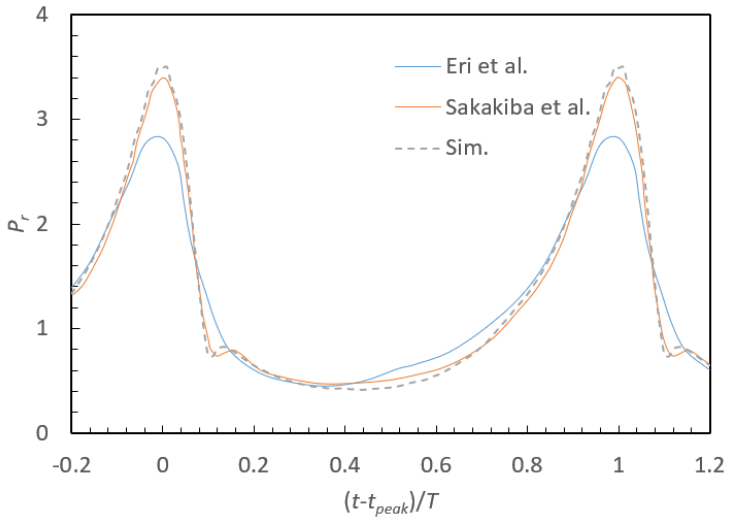

Figure 3.3. Normalized pressure of the simulation (Sim.) is compared with experiments with the two-orifice case at 100 Hz [54].

Time histories of P_r over two cycles are shown in Figure 3.4 and Figure 3.5 for f = 50 Hz, 75 Hz, 100 Hz, and 150 Hz for the two- and four-orifice models. There is only a minimal difference in the pressure variations for the two different cycles, indicating that a similar synthetic jet forms in each cycle. In addition, the pressure variations are highly asymmetric despite the piston movement described by the cosine function. The maximum pressure becomes larger as the frequency increases, and the minimum pressure becomes smaller. This is agreeing with the experimental results from Sakakibara et al. [53] for both two- and four-orifice cases.

LES for different frequencies indicates that, for a higher frequency, the pressure can attain the peak number in terms of later time (t_{peak}/T). For the two-orifice model, the values of t_{peak}/T and frequencies are (t_{peak}/T, f) = (0.365, 50 Hz), (0.399, 75 Hz), (0.420, 100 Hz) and (0.439, 150 Hz). For the four-orifice model, the values of t_{peak}/T and frequencies are (t_{peak}/T, f) = (0.275, 50 Hz), (0.305, 75 Hz), (0.360, 100 Hz) and (0.394, 150 Hz). As we can see, t_{peak}/T shift to the middle of the cycle as f

increases. The trend is the same in the case of a single orifice (as shown in Figure 2.5). In addition, by comparing the maximum pressure at a given frequency in Figure 3.4 and Figure 3.5, the maximum pressure in one cycle is more considerable when the total orifice area is smaller [53].

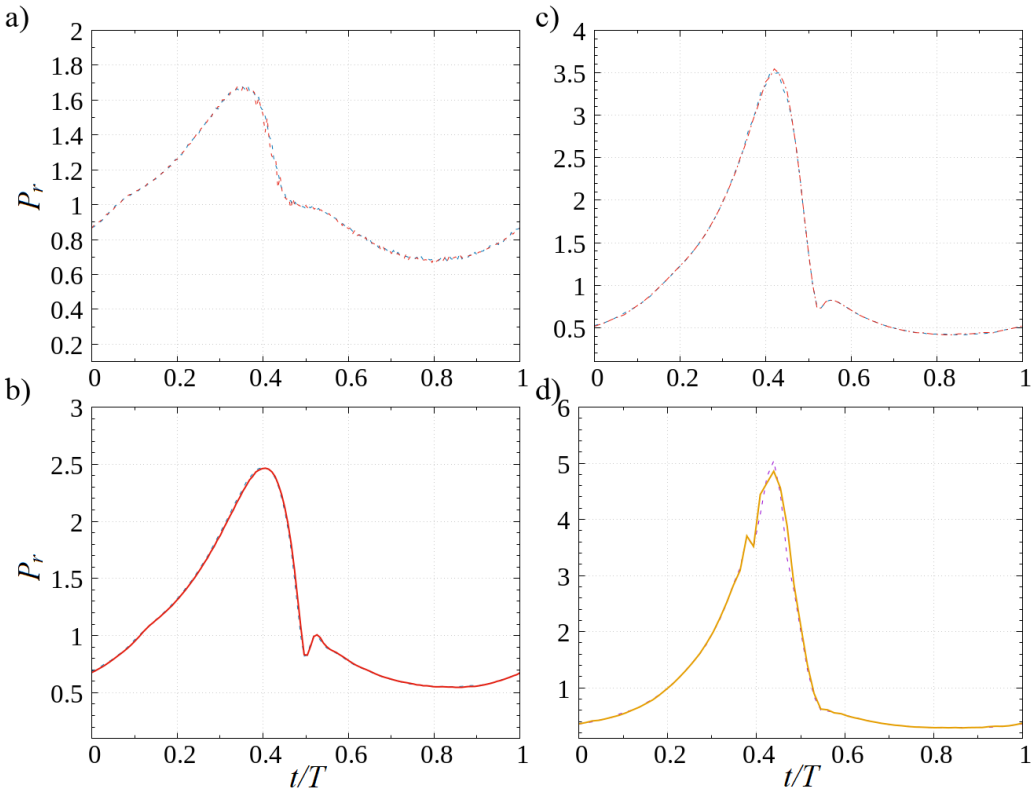

Figure 3.4. Normalized pressure P_r for different cycles (two-orifice model) of a) f = 50 Hz, b) f = 75 Hz, c) f = 100 Hz and d) f = 150 Hz.

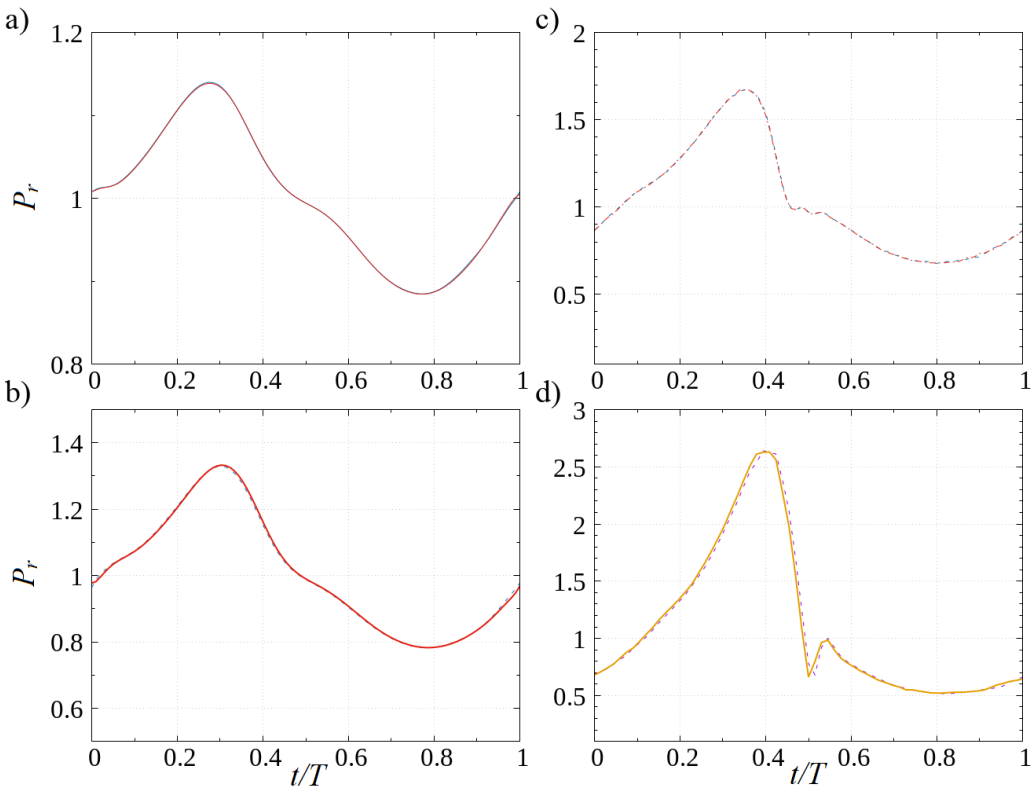

Figure 3.5. Normalized pressure P_r for different cycles (four-orifice model) of different frequencies (the order is same as in Figure 3.4).

Similar to Figure 2.7 in Chapter 2 about the single orifice, we compare the normalized pressure between the experiment and the simulation of two cases for two-and-four-orifice models, as shown in Figure 3.6 and Figure 3.7. In the same way, t - t_{peak} = 0, and 1 is when the pressure reaches the highest value in one cycle. These results also agree between the experiment and simulation.

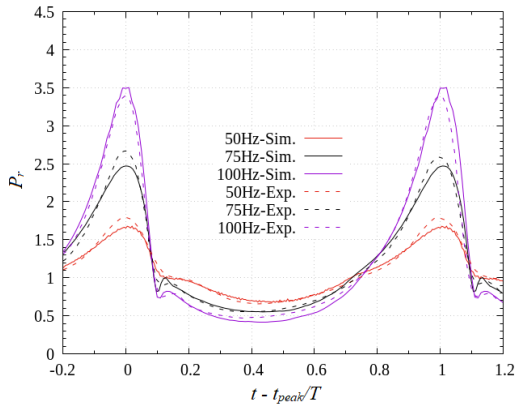

Figure 3.6. For two-orifice case, normalized P_r in comparison between experiment (Exp.) and simulation (Sim.)

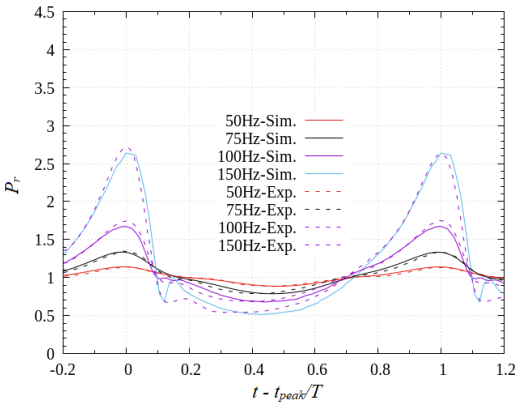

Figure 3.7. For four-orifice case, normalized P_r in comparison between experiment (Exp.) and simulation (Sim.)

3.3.2. Jet Mach Number History

The jet Mach number M is calculated as the same method in Chapter 2. The time histories of M for two- and four-orifice models are shown in Figure 3.8 and Figure 3.9. Here, the results for two cycles are shown for comparison. The Mach number variation hardly depends on the cycles, and the jet Mach number depends solely on the phases for each case. In the blowing phase, the Mach number increases with time and reaches the largest value. Then, it decreases with time until the end of the blowing phase. Finally, M slightly increases in the suction phase. The plots of M show that, at t/T = 0.5, the middle of the cycle is the transition time between the phases of blowing and ingesting. There are small effects of velocities in y-and z-directions so at t/T = 0.5, M is not exactly zero at higher frequencies. The Mach number is achieved at the maximum as follows: (t/T, f) = (0.375, 50 Hz), (0.406, 75 Hz), (0.430, 100 Hz) and (0.455, 150 Hz) for the two-orifice model. These times are respectively t/T = 0.305, 0.323, 0.360, and 0.410 for the four-orifice case. They closely approximate the instances when the pressure reaches its peak.

In short, in the frequency range in the present study, the Mach number depends on the frequency values. As the frequency increases, the maximum Mach number value also increases. This is related to the frequency dependence of maximum pressure. Also, based on a fixed value of frequency and no change in stroke length here, as the total orifice area increases, the maximum pressure value decreases due to more manageable air outflow during the piston movement. It also reduces the maximum Mach number value.

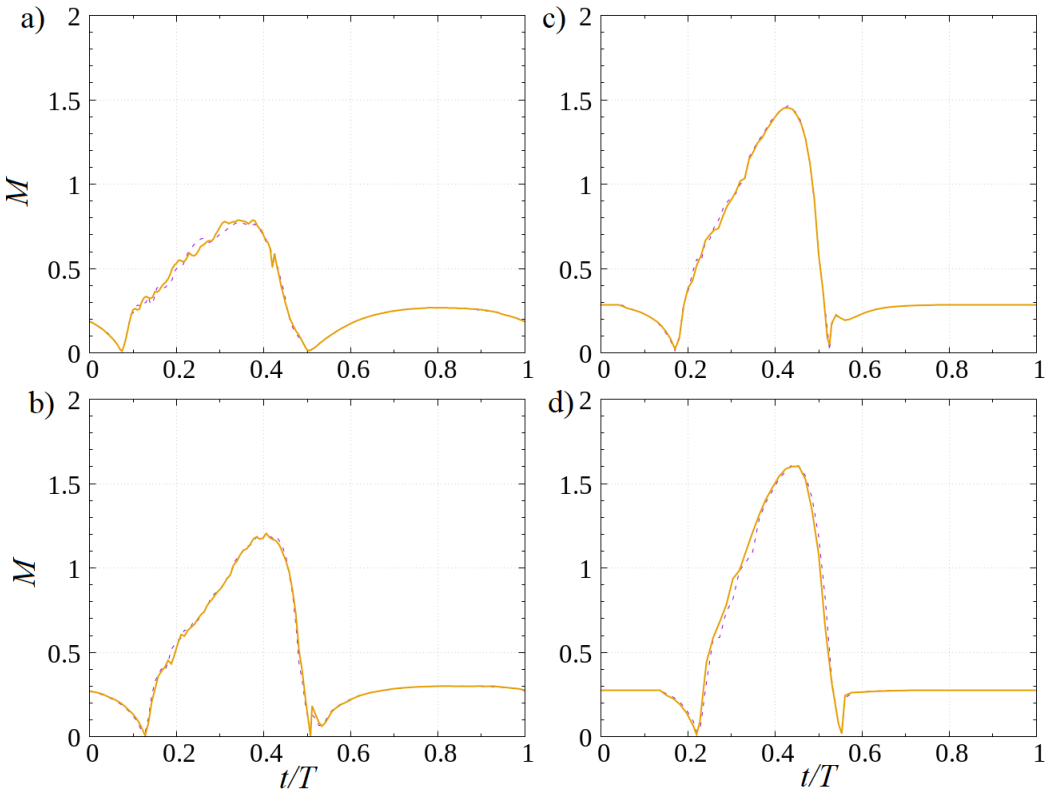

Figure 3.8. Mach number histories for the two-orifice model different frequencies (the order is same as in Figure 3.4).

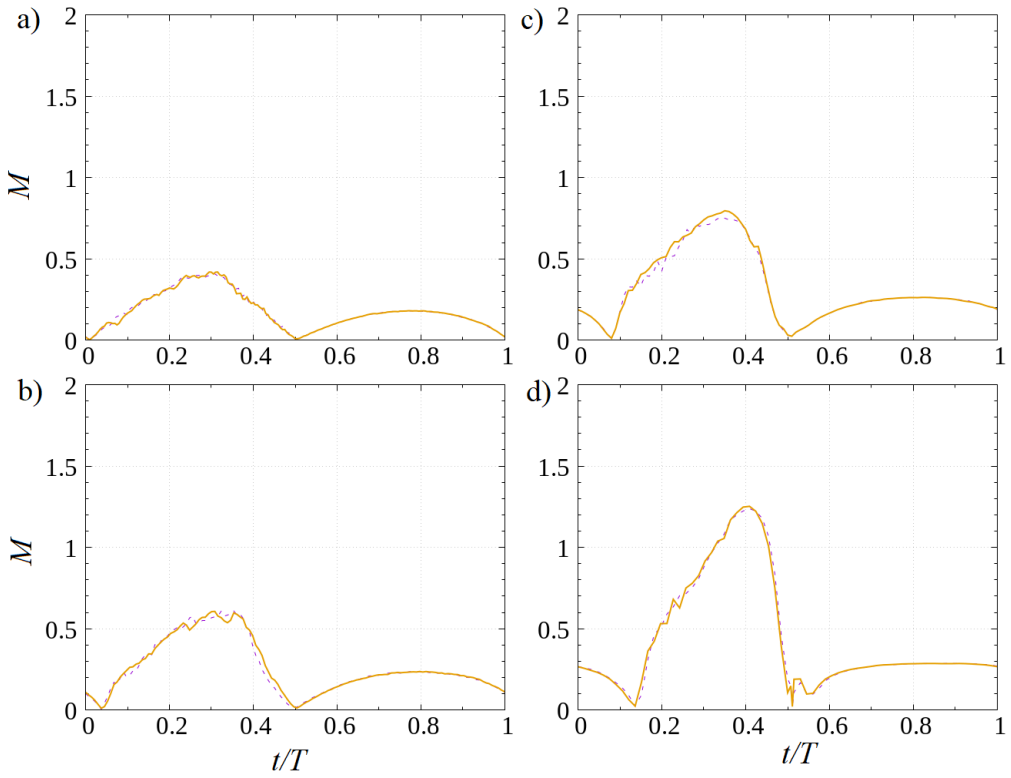

Figure 3.9. Mach number histories for the four-orifice model for different frequencies (the order is same as in Figure 3.4).

For a single-orifice case, the relation has been confirmed for the maximum Mach number M_{max} and the maximum pressure P_{rmax} [71]. Also, Figure 3.10 compares the present LES results of M_{max} and P_{rmax} for both cases of two-and-four orifice model. The Eq.(2.6) well describes the relation between M_{max} and P_{rmax} for multiple-orifice cases and proves beneficial in estimating the jet Mach number using pressure measurements.

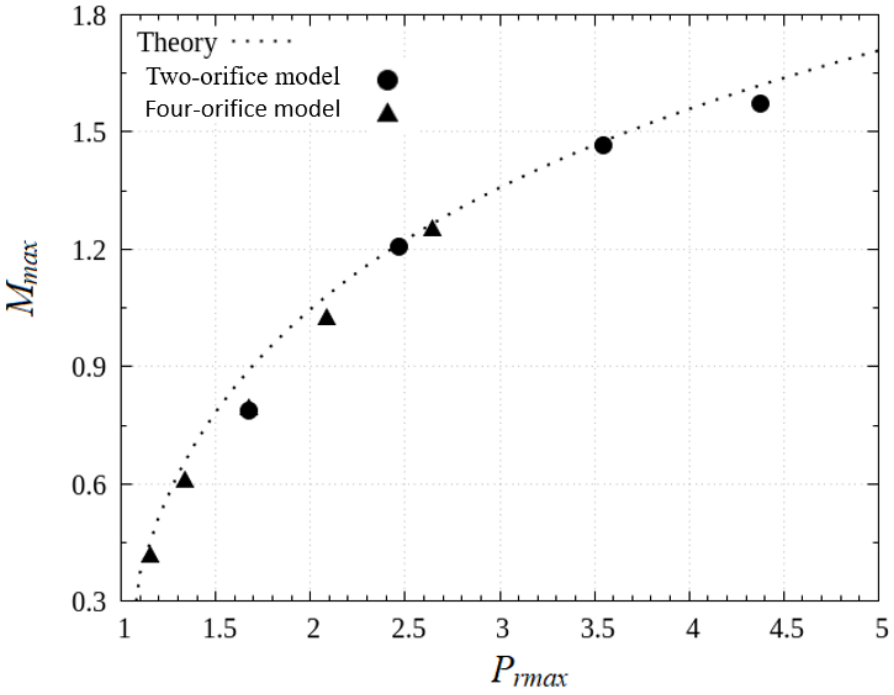

Figure 3.10. The maximum Mach number and pressure in correlation for the two-orifice model and the four-orifice model.

3.3.3. Phase-averaged Flow-field

In this section, we will discuss rms and velocity fluctuations defined with phase averages. The averages are evaluated as functions of time in the phase from t = 0 to T. In the streamwise direction, the phase-averaged velocity is denoted by U, while the rms value of velocity fluctuations, u_{rms}, are evaluated U as in the Chapter 2.

3.3.3.1. Two-orifice case

In the streamwise direction, Figure 3.11 presents the phase-averaged velocity on the plane that crosses the center of the orifices for f = 100 Hz. To evaluate the interaction between these two parallel jets, the phase-averaged velocity at the center line between these two jets is also shown in Figure 3.12. Here, y = 0 is the midpoint between the two orifices. The phase of blowing corresponds to t/T = 0.1—0.5 and while the phase of ingesting corresponds to t/T = 0.5—1. In Figure 3.11, we can observe the growth of the jets in the blowing phase. The two jets tend to interact to form a converging region, then create a merging region where they meet each other, and become a single jet in a combined region. A similar transition was also found for two continuous parallel jets [36]. The converging region is observed near the orifice when the velocity of the jets is high, e.g., $x/d \lesssim 5$ at t/T = 0.4, where the mean velocity increases with x along the centerline in Figure 3.12 d. The flow induced by a PSJA with two round orifices was visualized with a shadowgraph technique [53]. They also observed that the converging region forms for $x/d \lesssim 5$ for the case of two-orifice jets at 100 Hz. For the present LES, the merging region falls within the approximate range of $5 < x/d < 17$. At an early time in the cycle, when the jets are being formed in Figure

3.11 b-c, with the streamwise direction, the two jets align and spread in the vertical direction resulting in the interaction of the jets. At a later time, the jets are inclined to the other jet in Figure 3.11 e, resulting in the formation of the merging and combined regions. Because the inclination of the jets occurs at a late time of the blowing phase, the merging region and combined region move with time. In Figure 3.11 e, the jets merge at about x/d = 25. The inclination of the jets causes the converging and merging regions to be closer to the orifices. In Figure 3.12 e, the converging region already appears at about x/d = 2. Figure 3.12 indicates that the mean velocity along the centerline between the orifices reaches 250 m/s at the maximum. The increase of the mean velocity with x also confirms the formation of the merging and combining regions in Figure 3.12 b-e. In Figure 3.12 a, a negative mean velocity is observed near the wall related to the flows into the orifices from outside. Thus, the induced flow in the suction phase still affects the flow at the moment when the piston is going upward. After t/T = 0.5, the flow toward the top wall of the PSJA is observed as a negative mean velocity. However, this velocity is smaller than the mean velocity in the blowing phase.

Figure 3.13 plots u_{rms} on the same centerline as in Figure 3.12. The merging and combined regions have a large mean velocity during the blowing phase in Figure 3.12 b-e. The regions with large u_{rms} in Figure 3.13 b-e approximately agree with those with a large mean velocity of the merging region and combined region, and the interaction of the two synthetic jets causes large velocity fluctuations. The rms velocity fluctuations reaches the maximum of 80 m/s, which is expected to be large enough for fluid compression and expansion due to turbulent motions to affect the flow. As also found for the mean velocity, u_{rms} in the suction phase is very small. As

the jet entrains ambient fluid, momentum is transferred from the jet to the surrounding. This momentum exchange affects the flow patterns and velocity distribution in the vicinity of the jets as well as overall flow behavior. Figure 3.9 d and e show the core jets with the highest velocity and the effect of the increasing ambient velocity. In addition, the momentum transport due to jets obeys the momentum conservation principle, which is applied to the computational domain with zero-net-flux-mass jet. According to this principle, the total momentum in a system remains constant unless acted upon by external forces. Therefore, the momentum carried by the jets is transferred to the surrounding fluid, altering the overall momentum distribution and potentially inducing flow acceleration.

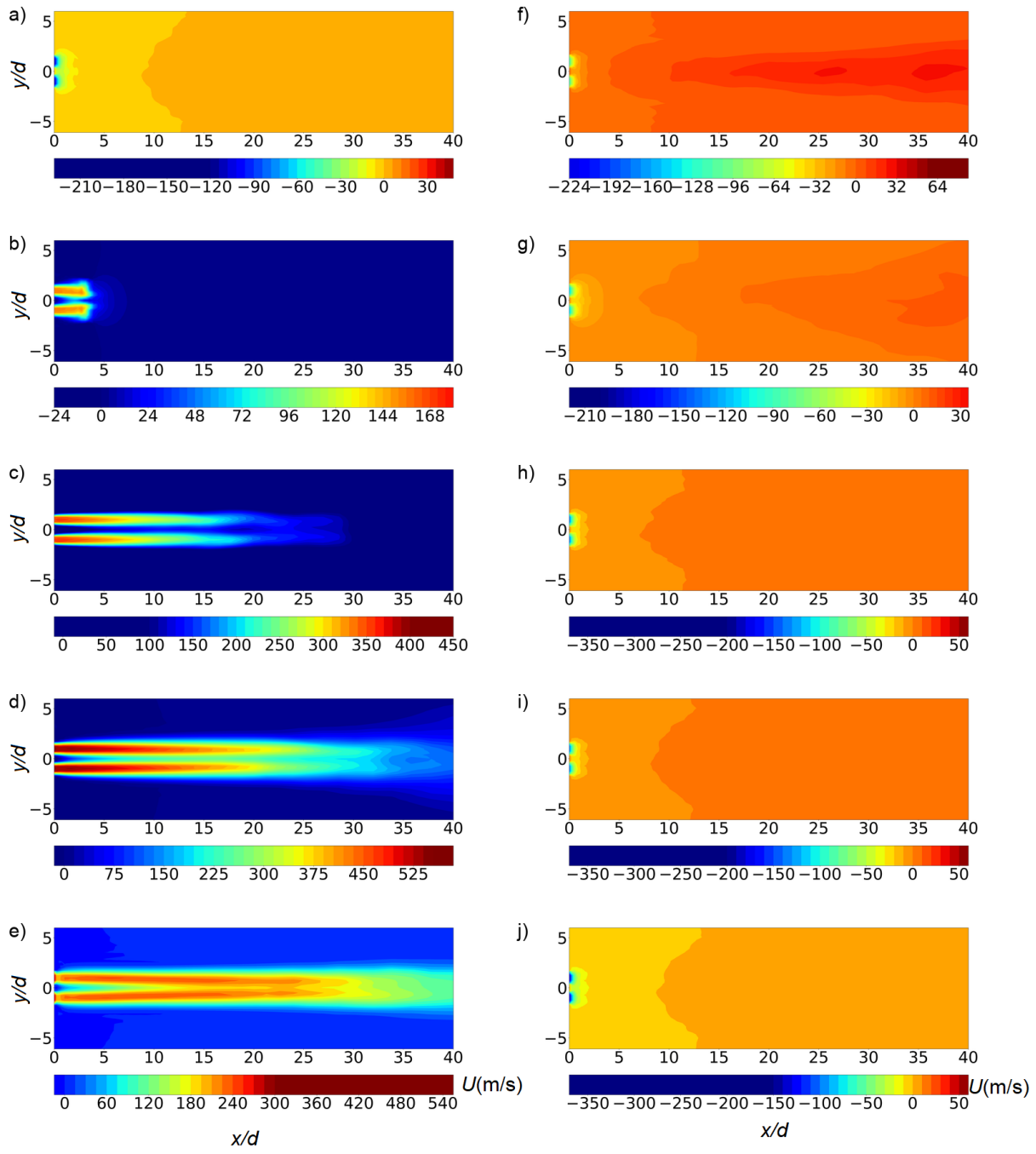

Figure 3.11. For f = 100 Hz with t/T from 0.1 to 1 by increment of 0.1 for a-j, phase-averaged velocity field is visualized in the streamwise direction (two-orifice model).

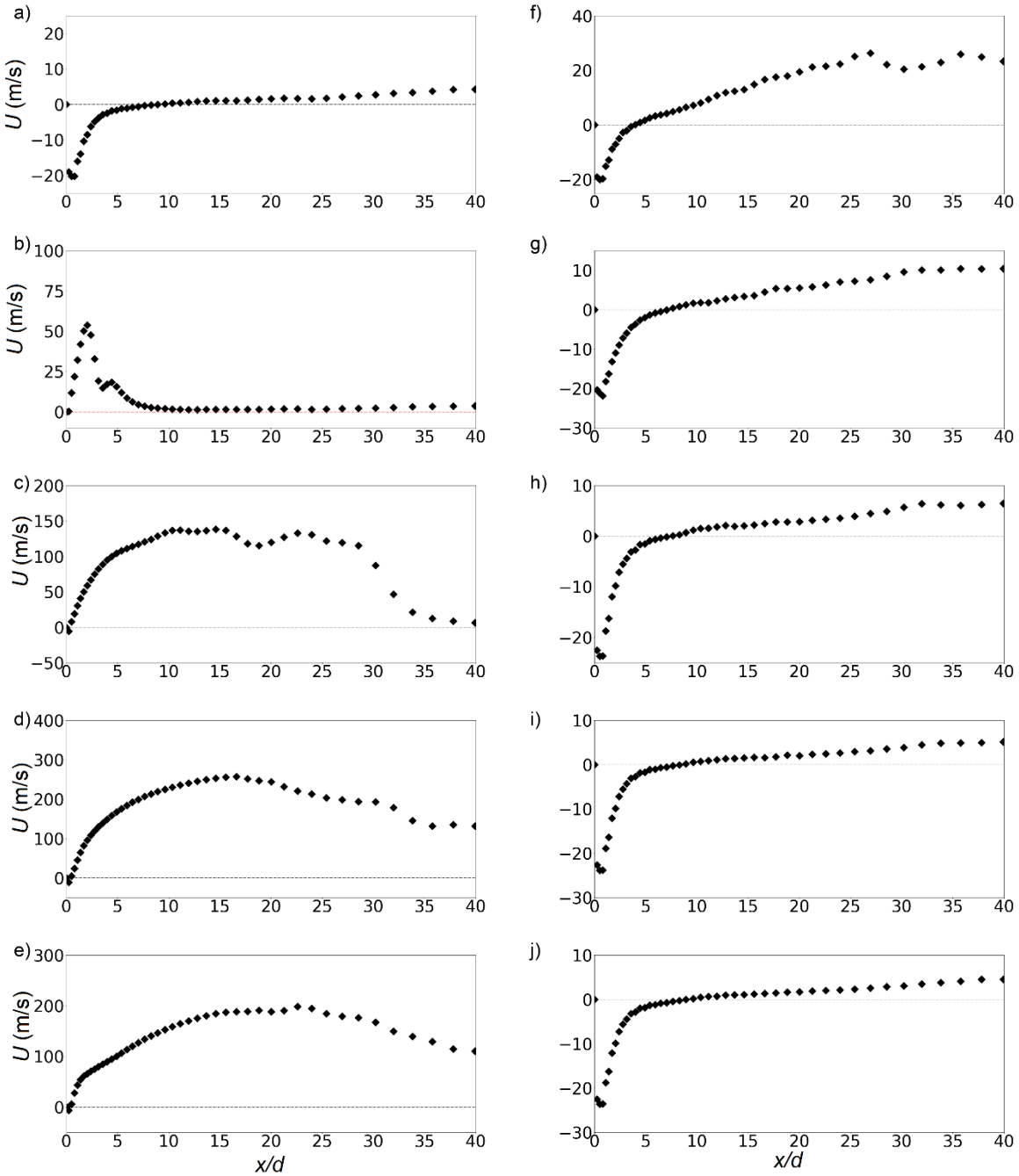

Figure 3.12. Centerline phase-averaged velocity in the streamwise direction for the two-orifice model (the frequency and order are same as in Figure 3.11).

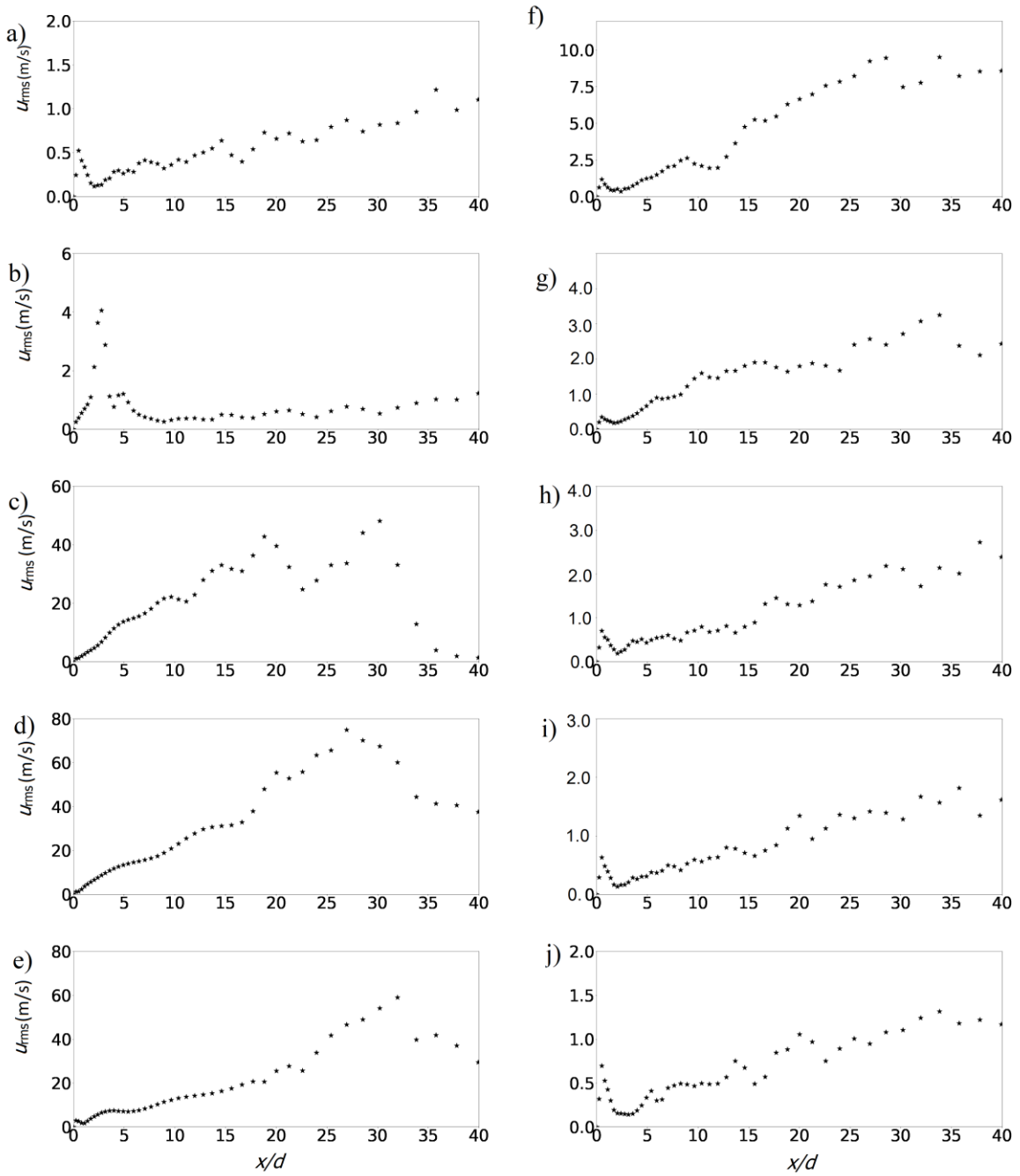

Figure 3.13. The root-mean-square (rms), u_{rms}, along the centerline of velocity in the streamwise direction of the two-orifice model (A-A plane in Figure 3.1 a) of the two-orifice model (the frequency and order are same as in Figure 3.11).

3.3.3.2. Four-orifice case

The rms velocity fluctuations and mean velocity are presented at the center of four orifices, i.e., the C-C plane in Figure 3.1 b. The results for the four-orifice model are also presented for f = 100 Hz. For this case, the maximum Mach number is about 1, which is smaller than that for the two orifices with the same frequency because of the difference in the total orifice area.

Figure 3.14 shows the phase-averaged velocity from t/T = 0.1 to 1.0 for the four-orifice model. Because the C-C plane does not pass through any orifice, the velocity also asymptotes to 0 toward x = 0, which is the top surface of the PSJA. The interaction of the four jets induces the mean velocity on this plane in the blowing phase (Figure 3.14 b-e). At the end of the blowing phase in Figure 3.14 e, the four jets are fully combined forming a single jet with a large mean velocity along the centerline. The jets have not fully merged yet at an early time in Figure 3.14 b-d, where the large mean velocity in each jet can be identified. This time-dependent behavior of the jet interaction is generally in good agreement with the two orifices model. This merging point occurs downstream of the converging points and is influenced by the velocities. The merging point in a two-orifice case is where the flows from the two orifices join together and form a combined flow. In a four-orifice case, there are four orifices from which the jets are generated. The converging and merging points refer to the locations where the individual jets from different orifices come together and interact. Due to multiple orifices, there can be several merging points where the interactions between the jets occur. These merging points can occur simultaneously because the distance between each pair of the jet is the same.

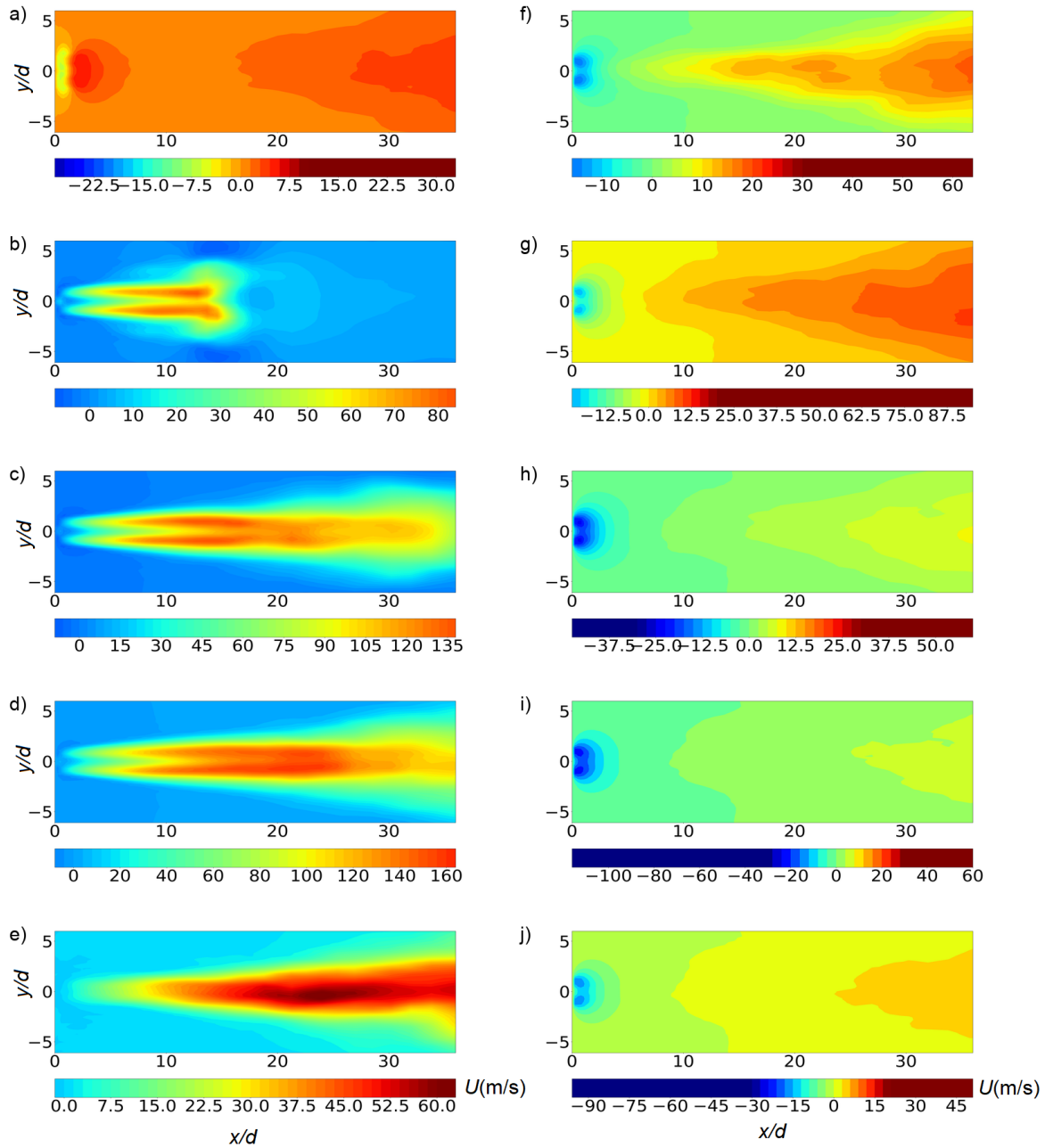

Figure 3.14. For f = 100 Hz with t/T from 0.1 to 1 by increment of 0.1 for a-j, phase-averaged velocity field is visualized in the streamwise direction at C-C plane in Figure 3.1 b for the four-orifice model.

Figure 3.15 shows the rms velocity fluctuations along the centerline of the four orifices. At t/T = 0.2, the mean velocity decreases at about x/d = 14 in Figure 3.14 b. The rms fluctuations also become small beyond this location. Therefore, the fluctuation of velocity exhibits significant magnitude at the streamwise end of the jets. For t/T = 0.3—0.5, the rms fluctuations tend to increase with x. This will be explained in the next section with the instantaneous velocity profile. In the suction phase, as x/d increases, rms fluctuations also tend to grow, as expected from the remnant of the jets generated in the blowing phase. The rms velocity fluctuations for the four-orifice model are smaller than those for the two-orifice model. In continuous jets, the magnitude of velocity fluctuations depends on the initial jet velocity. The present comparison for the two- and four-orifices models is for the same frequency of 100 Hz, which results in a smaller velocity at the orifice for the four-orifice model. This difference causes the small rms velocity for the four-orifice model.

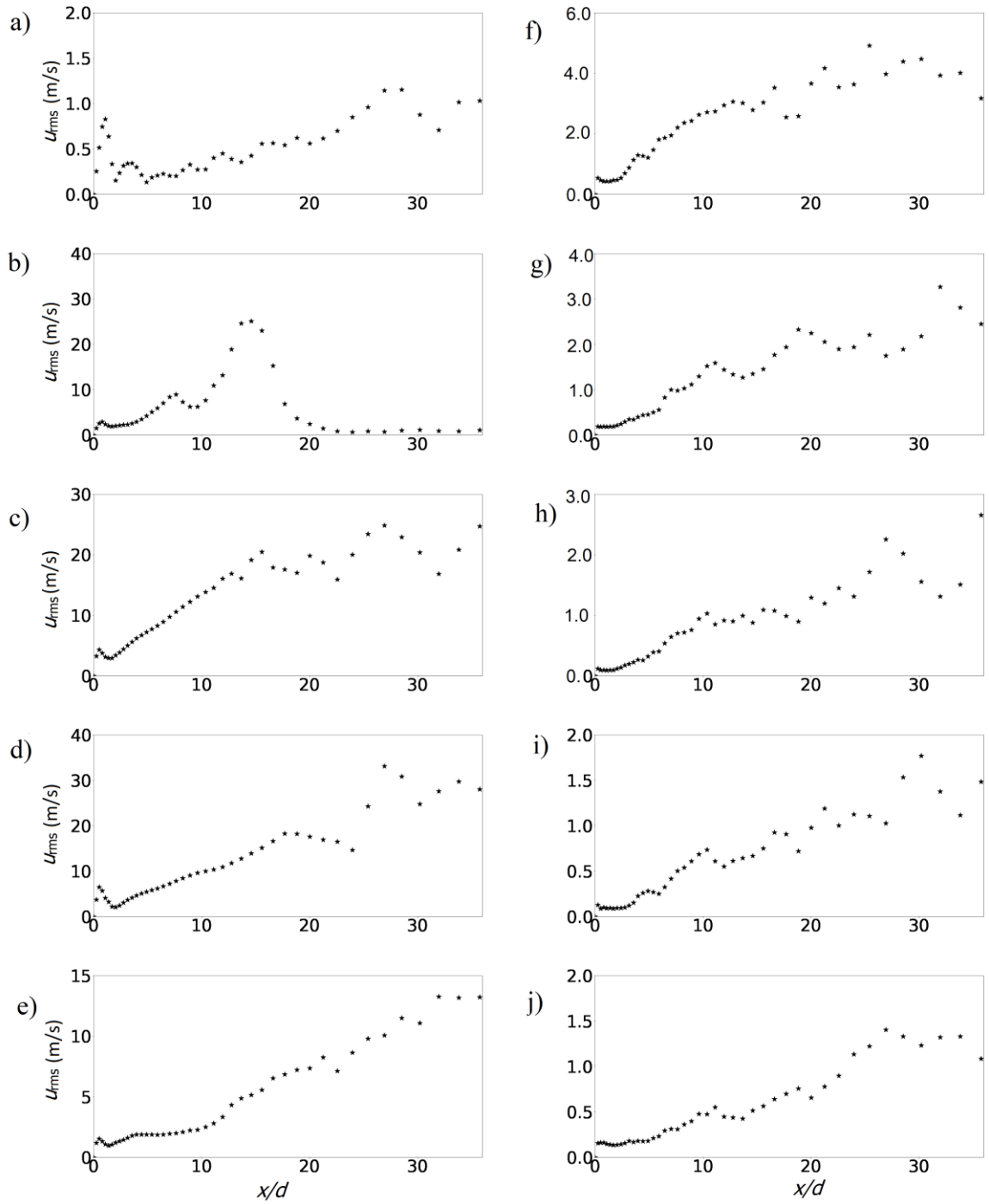

Figure 3.15. The root-mean-square (rms), u_{rms}, along the centerline of velocity in the streamwise direction of the two-orifice model (C-C plane in Figure 3.1 b) of the four-orifice model (the frequency and order are same as in Figure 3.14).

For more details of the maximum rms values, Figure 3.16 plots u_{rms} at t/T = 0.4 and 0.5, focusing on the profiles far downstream from the orifice exit. For t/T = 0.4, the rms reaches its maximum value at x/d = 28 (Figure 3.16 a); for t/T = 0.5, the maximum rms is obtained at x/d = 48 (Figure 3.16 b). When comparing positions of the maximum rms values, the trend is similar to the two-orifice case, i.e., the position of the maximum rms of t/T = 0.5 is further downstream than that of t/T=0.4. Furthermore, here in the case of the four-orifice interaction, the position of the maximum rms is further downstream due to the interaction of the four orifices.

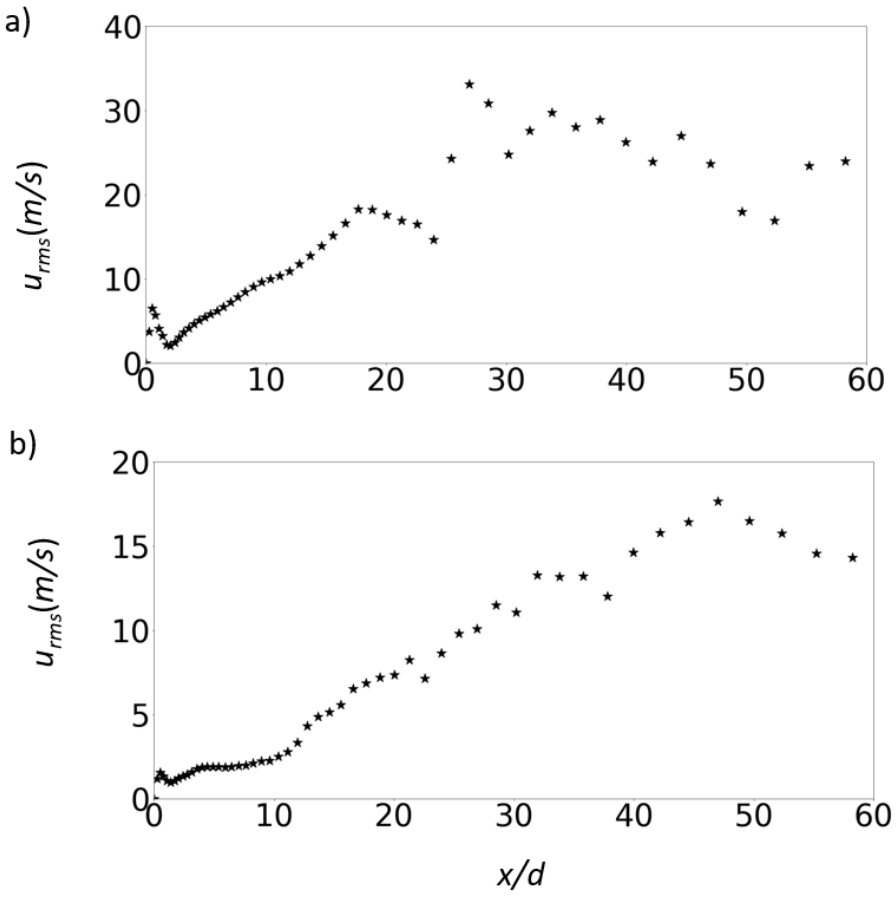

Figure 3.16. Same conditions as Figure 3.15 a) a) t/T = 0.4, b) 0.5.

Figure 3.17 presents the flow field along the centerline of the jet plane (B-B) of the four-orifice model t/T=0.4. The jet converging region is observed for $x/d < 2$, as seen in Figure 3.17 a. In addtion, because velocity in the x-direction is zero (in Figure 3.17 b), it is also a sign of converging [36]. Before the jet converging region, flow is quasi-laminar state, where rms velocity is small. At the same time, in this region, the turbulent intensity, which is the ratio between rms velocity and the mean velocity, decreases significantly caused by the increase in the mean velocity, as shown in Figure 3.17 c. However, it reaches an almost contant value of 0.2, which is closet to a typycal value of a continuous round jet [73]. In addition, phase-averaged pressure non-dimensilnalized by the atmosphereic pressure, $P_{rp,}$ shown in Figure 3.17 d, increases in the x direction from x/d = 0 to 2. This pressure gradient can cause the flow toward the orifice plate, producing the recirculation zone occurs here, as further examined below.

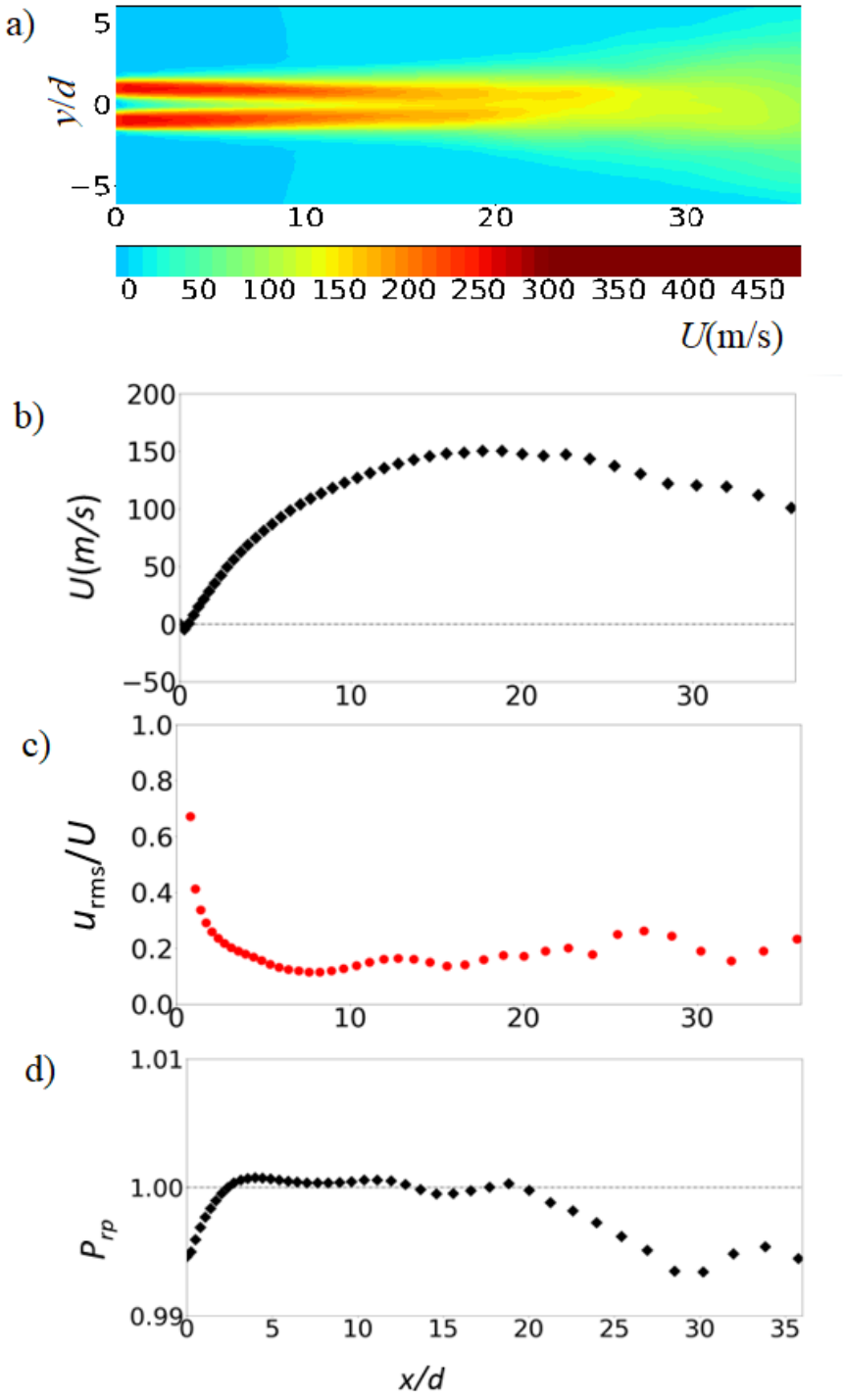

Figure 3.17. At t/T= 0.4, flow field (a), streamwise distributions of mean velocity (b), turbulent intensity (c), and mean pressure (d) on along the centerline of B-B plane (jet plane). The statistics are defined with phase averages.

Figure 3.18 shows the time-averaged streamwise velocity along the centerline of the two-orifice case (f = 100 Hz). A long the centerline, the mean velocity is negative near the orifice (about $x/d < 1$), rapidly increases with x up to about $x/d = 5$, and varies slowly with x for the further downstream region. One of the crucial parameters for the synthetic jet interaction is the ratio R [74] between the orifice spacing and side length of the orifice, which is 2 for the present two-orifice model. The interaction of two low-speed synthetic jets was investigated by Kim et al. [74], where one of the experiments also considered $R = 2$. The present result is similar to their experimental results. They also observed a negative mean streamwise velocity along the centerline near the orifice (about $x/d < 1.4$) and a rapid increase with x up to about $x/d = 6$. The distribution of the mean velocity strongly depends on turbulence, as the Reynolds stresses due to velocity fluctuations significantly contribute to the momentum flux, which is dominated by large-scale velocity fluctuations. The agreement with the experiments suggests that the large-scale turbulent motions are accurately simulated in the present LES and that the jet interaction is similar for both high-speed and low-speed synthetic jets.

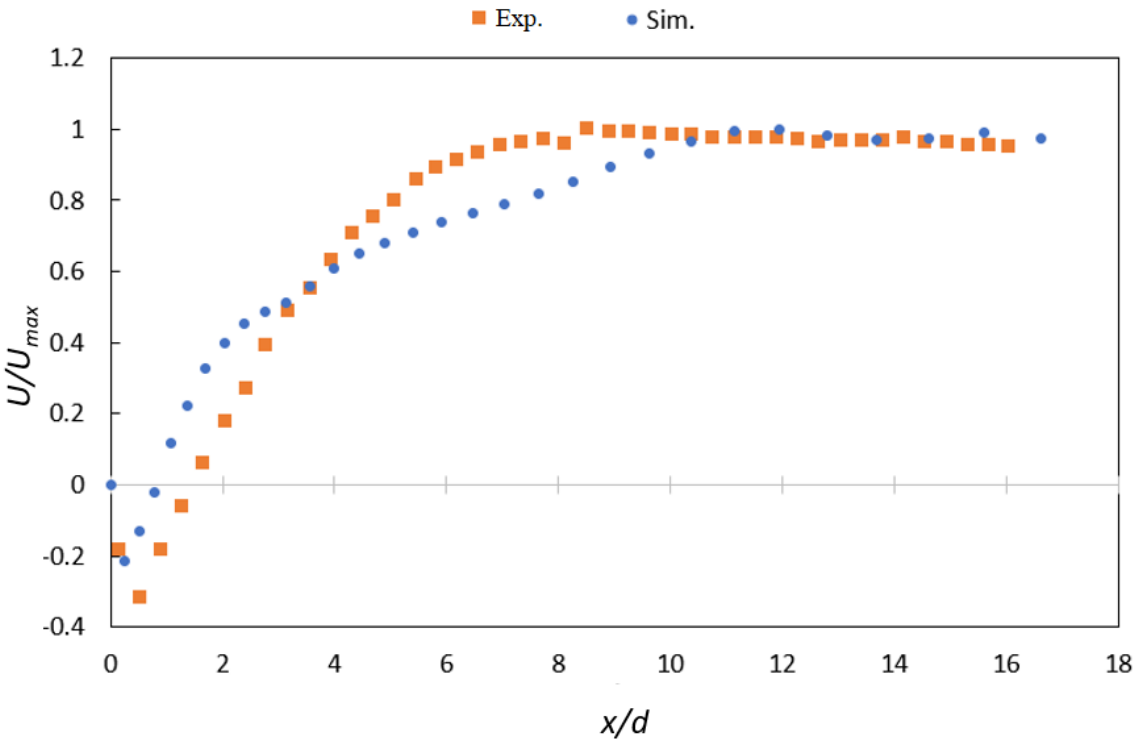

Figure 3.18. Time-averaged streamwise velocity along the centerline for the two-orifice model between the simulation and experiment [74]。

3.3.4. Instantaneous velocity magnitude

Figure 3.19 shows the instantaneous profiles of velocity magnitude at the A-A plane of the two-orifice model in Figure 3.1 a at t/T = 0.4 and 0.5, for which the mean velocity and rms velocity fluctuations are shown in Figure 3.12 d, Figure 3.12 e, Figure 3.13 d, and Figure 3.13 e, respectively. The phase-averaged velocity reaches its maximum value at around x/d = 15~16. However, in Figure 3.13 d, rms fluctuations attain their maximum value at about x/d = 26. In Figure 3.19 a, x/d = 26 roughly corresponds to the position of the end of the merging region, where the value of rms fluctuations significantly increases due to the jet interaction. This is also shown similarly when we compare Figure 3.13 e and Figure 3.19 b: the maximum value of rms fluctuations is observed at about x/d = 32, which corresponds to the end of the merging region in the instantaneous velocity profile. We have also observed a similar tendency for the jet merging point and the rms velocity fluctuations for the four-orifice model.

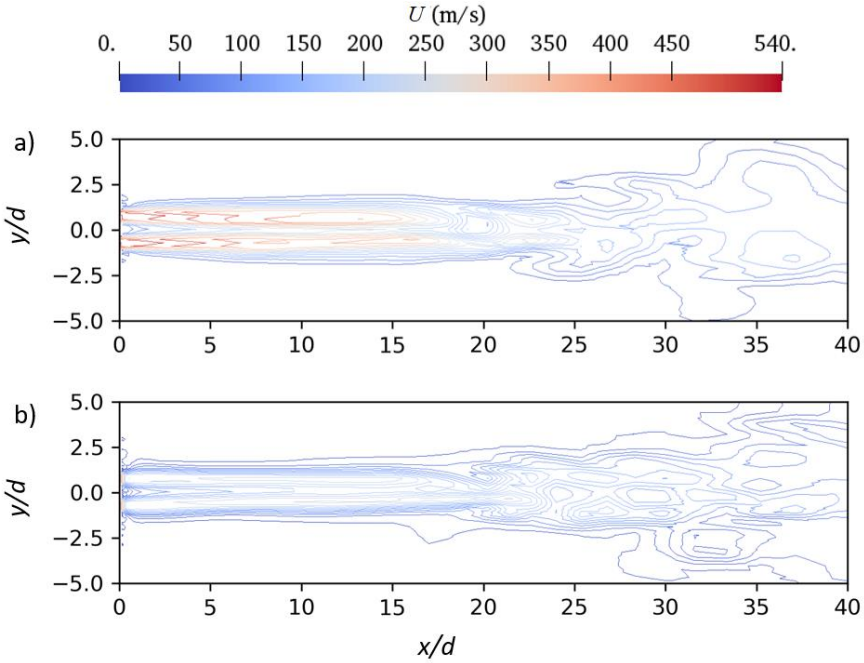

Figure 3.19. Instantaneous distribution of the velocity magnitude on the A-A plane of the two-orifice model at a) t/T = 0.4 and b) t/T = 0.5.

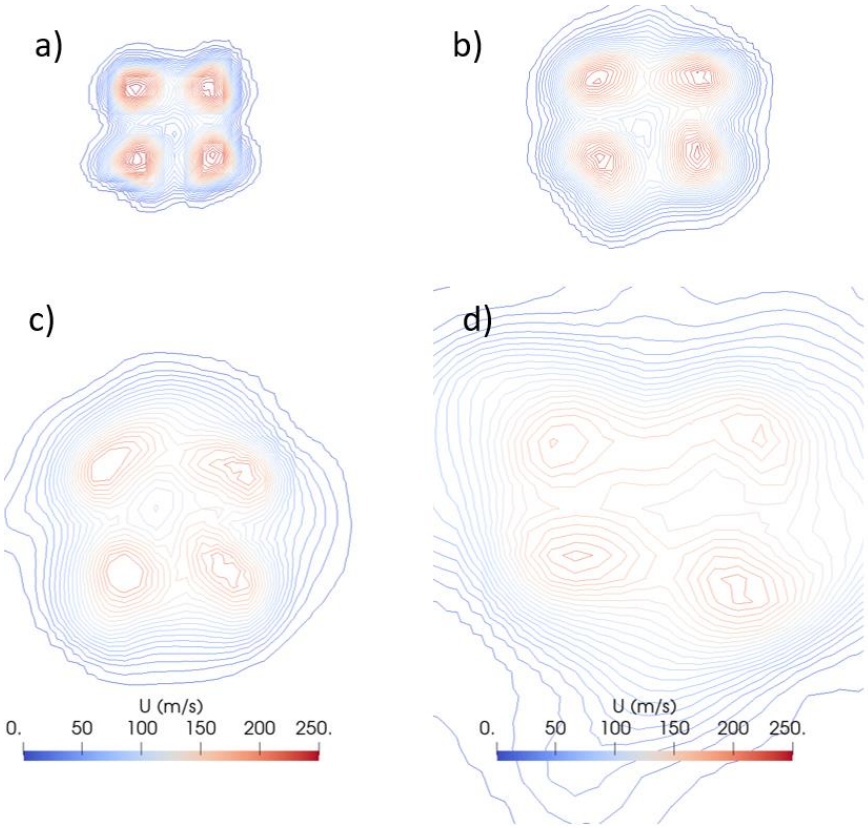

Figure 3.20. Instantaneous velocity magnitude of four-orifice case with f = 100 Hz at x/d = a) 5 b) 10 c) 15 d) 20.

Figure 3.20 shows the instantaneous velocity of the four-orifice case with different locations in the *x*-direction at $t/T = 0.4$, at $x/d = 5$, 10, 15, and 20. Four jet cores are formed near the orifice, and the distance between them increases as x/d increases. The similar velocity contour is also formed in the middle of the four jet cores at $x/d = 5$, 10, and 15. When $x/d = 20$, this contour is no longer clear. This indicates the preparation for the formation of the merging zone.

3.3.5. PDF of velocity fluctuations

The probability density function (PDF) of velocity fluctuations u' from the phase-averaged velocity is evaluated on the centerline of the flow at x/d = 5, 10, and 15. Hereafter, the PDF is normalized by the rms velocity fluctuations. Figure 3.21 plots the PDF for the two-orifice model at t/T = 0.4 and 0.8, which are in the blowing and suction phases, respectively. The position is of taken data: (x/d, y/d) = (5,0), (10,0), (15,0) in Figure 3.19 a, where located before combing region (as show in Figure 3.11 d). In this region, two-jets' structures with high velocity slow down the flow movement between them, which may result a negative velocity fluctuation. For comparison, a Gaussian distribution for the PDF is shown with a broken red line in each figure. Although scatters are not negligible because of the limited number of samples, the distribution is still useful to discuss a general trend of the deviation from the Gaussian function. In the blowing phase of t/T = 0.4, a peak of the PDF appears for $u' > 0$, and the distribution deviates from the Gaussian function. Here, the PDF is negatively skewed, and a very large reversal velocity is observed at a low probability. A similar deviation of a PDF of velocity fluctuations was also reported for the interaction of continuous jets, even though a fully developed single jet has a Gaussian PDF along the jet centerline [39]. The PDF in the suction phase of t/T = 0.8 is closer to the Gaussian function than that in the blowing phase. Therefore, the suction due to the PSJA does not induce extremely large velocity fluctuations. Figure 3.22 shows the PDF for the four-orifice model along the centerline. Unlike the two-orifice model, the PDF is positive skewed for the four-orifice model, and the flow caused by the interaction of four synthetic jets does not accompany by very large negative velocity

fluctuations. Areas near the center line of the single orifice jet with the same location as above can also tend to have the PDF like two-orifice case because of the high velocity of the jet. For a fixed frequency, the flow generated by the two-orifice model has stronger intermittency in the blowing phase than that for the four-orifice model because of higher probability of having relatively low-velocity fluctuations compared to high-velocity fluctuations. This intermittent behavior results in a skewed distribution of the PDF.

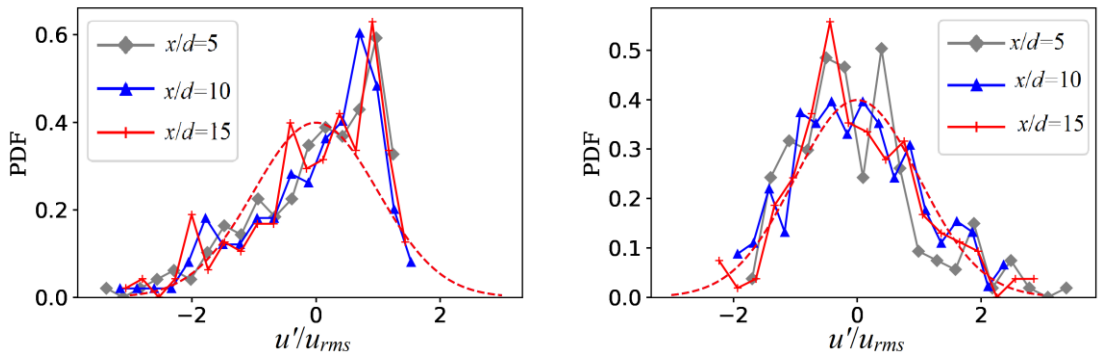

Figure 3.21. PDF of u'/u_{rms} at x/d = 5, 10, and 15 along the centerline of the PSJA for the two-orifice model: a) t/T = 0.4 and b) t/T = 0.8. A red broken lines represents a Gaussian distribution.

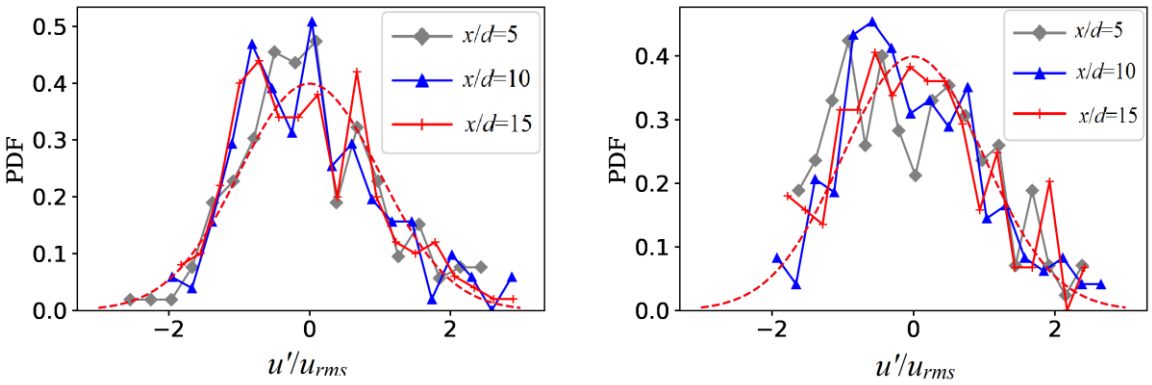

Figure 3.22. Same as Figure 3.21 but for the four-orifice model.

3.4. Concluding remarks

The flow properties of the piston synthetic jet actuator (PSJA) with two and four orifices are investigated with LES. The flow generated by the PSJA with multiple orifices is examined for a wide range of actuation frequencies. Regardless of the number of orifices and the frequency, temporal variations of the pressure within the actuator and the Mach number are almost identical for different cycles, confirming that the jets are repeatedly generated under the same conditions. The maximum jet Mach number observed in the blowing phase is related to the maximum pressure inside the actuator, and their relationship for both two- and four-orifice models is well described by the theory for a flow inside a nozzle.

The interaction of synthetic jets generated by the two- and four-orifice models is investigated with the statistics conditioned on the phase. Slightly before the ending of the blowing phase, the typical three regimes of the interaction reported for continuous jets [36] are observed for the synthetic jets: the converging region, where the jets are inclined toward the other jets; the merging region, where the synthetic jets interact; a combined region with a single jet formed from the multiple synthetic jets. Due to the time-dependent feature of the synthetic jets, the locations of these regions vary with time. Specifically, the jets tend to be parallel to each other at the beginning of the blowing phase, for which the converging region is not clearly observed. Therefore, the jets are not combined until a later stage of the blowing phase. These features are observed for both two- and four-orifice models. At the beginning of the blowing phase, near the furthest locations where the jets reach, the rms of velocity fluctuations is significant. However, once the interaction of the synthetic jets occurs,

large rms velocity fluctuations are observed at the downstream end of the merging region. As the merging region is shifted toward the downstream region with time in the blowing phase, the location where the rms velocity fluctuations attain the maximum also varies with time. We have also examined the PDF of velocity fluctuations. However, the deviation of the PDF from a Gaussian function is not significant for the suction phase. The present results for the interaction of the synthetic jets generated by the PSJAs will be useful for future applications in developing devices for flow control and the facilities to generate compressible turbulence.

CHAPTER 4. CONCLUSIONS

The basic characteristics of piston-driven synthetic jets are studied through large eddy simulation (LES). Two types of PSJ, which are single-orifice jets and multi-orifice jets, were performed by this simulation. By numerical means, the flow fields of the PSJs are clarified. In the case of multi-synthetic jets, two-and-four jets are studied. The computational outcomes are verified against the experimental data and demonstrate a strong correlation. The main findings in Chapter 2 and Chapter 3 are summarized based on this research objectives.

Firstly, there are common points to both single-and-multi orifice jets simulations. For the two fundamentally important parameters, the pressure within the cylinder and the Mach number, temporal variations are almost identical for different cycles. When increasing frequency f during one cycle, the minimum pressure contracts as the maximum pressure expands. In addition, the maximum Mach number can be effectively described in the relationship with the maximum pressure. In addition, their relationship demonstrates consistency alongside the theoretical prediction.

In the case of a single orifice jet, the dependence of PSJ on frequency is verified. Specifically, synthetic jets can become supersonic flow in both the flowing and suction phases when frequency f is greater than 100 Hz. When frequency f is large enough, the jet behavior will depend less on frequency f. Regarding the flow field, the high turbulence level is at the furthest point of the jet, where the flow velocity decreases.

The interaction of high-speed synthetic jets is investigated, giving rise to the emergence of converging, merging, and combined regions akin to those observed in continuous jets. The phenomenon occurs slightly before the end of the blowing phase. Once the jets merge through mutual interaction, significant fluctuations in velocity become apparent at the downstream extremity of the merging region. Along the center line of the jets, the probability density functions of velocity fluctuations exhibit a propensity to deviate from a Gaussian distribution during the blowing phase. This deviation is more pronounced in the two-orifice model than in the four-orifice model, while both models operate at the same frequency.

CHAPTER 5. FUTURE PROSPECTS

The interaction between a synthetic jet or arrays of jets and an external cross flow over the surface on which they are installed has the ability to alter the nearby streamlines and create a modification in the surface shape. This phenomenon holds significant importance in the field of flow control applications [18]. Because of the complexity of this interactive phenomenon, for example, the vortical structure [75], it has implications for both basic research and applications. Comparisons between synthetic jet and continuous jet in crossflow were also studied, and show similar results about mean velocity and turbulence intensity [76]. Properties of reversed flow and vortex pair are explored. The process of formation and decay is closely related to jet momentum [77].

Through the characteristics of conventional jets with crossflow, it raises some similar questions with high-speed synthetic jets. The current research related to this issue still requires to be investigated. Therefore, prospects can go in two main directions.

1. The interaction between single PSJ and cross flow.
2. Interaction between PSJ array and cross flow.

References

[1] Gad-el-Hak, M., Pollard and A., Bonnet, J., "Flow control: fundamentals and practices," *Springer*, (1998).

[2] Lin., J.C., "Review of research on low-profile vortexgenerators to control boundary-layer separation," *Progress in Aerospace Sciences*, vol. 38, pp. 389-420, (2002).

[3] Gao, L., Zhang, H., Liu, Y., and Han, S., "Effect of vortex generators on a blunt trailing-edge airfoil for wind turbines," *Renewable Energy*, vol. 76, pp. 303-311, (2015).

[4] Mueller-Vahl, H., Pechlivanoglou, G., Nayeri, C. N. and Paschereit, C. O., "Vortex generators for wind turbine blades: a combined wind tunnel and wind turbine parametric study," *Proceedings of ASME Turbo Expo*, pp. 899-914, (2012).

[5] Buder, U., Petz, R., Kittel, M., Nitsche, W. and Obermeier, E., "AeroMEMS polyimide based wall double hot-wire sensors for flow separation detection," *Sensors and Actuators A*, vol. 142, pp. 130-137, (2008).

[6] Cattafesta III, L. N. and Sheplak, M., "Actuators for active flow control," *Annual Review of Fluid Mechanics*, vol. 43, pp. 247-272, (2011).

[7] Sato, M., Okada, K., Asada, K., Aono, H., Nonomura, T. and Fujii, K., "Unified mechanisms for separation control around airfoil using plasma actuator with burst actuation over Reynolds number range of 10^3-10^6," *Physics of Fluids*, vol. 32, pp. 025102, (2020).

[8] Zainuddin, F.A., and Daud, N.M., "A review on dielectric darrier discharge (DBD)

plasma actuator in aeronautics applications," *Journal of Advanced Research in Fluid Mechanics and Thermal Sciences*, vol. 2, pp. 125-132, (2018).

[9] David, K., David, H. and David, G., "Plasma actuator application on a full-scale aircraft tail," *AIAA Journal*, vol. 57, no. 2, pp. 1-12, (2019).

[10] Santhanakrishnan, A. and Jacob, J. D., "Flow control with plasma synthetic jet actuators," *Journal of Physics. D: Applied Physics*, vol. 40, no. 3, pp. 637-651, (2007).

[11] Dahalan, M.N., Zahari, H., Abdul-Latif, A., Mat, S., Mansor, S., Othman, N., Wahid, M.A., Omar, W.Z.W., Ali, W.K.W., Lazim, T.M. and Nasir, M.N., "Feasibility study of plasma actuator for flow separation control," *Journal of Advanced Research in Fluid Mechanics and Thermal Science*, vol. 2, pp. 201-212, (2020).

[12] Thomas, F. O., Corke, T. C., Iqbal, M., Kozlov, A. and Schatzman, D., "Optimization of dielectric barrier discharge plasma actuators for active aerodynamic flow control," *AIAA Journal*, vol. 47, no. 9, pp. 2169-2178, (2009).

[13] Jolibois, J. and Moreau, E., "Enhancement of the electromechanical performances of a single dielectric barrier discharge actuator," *IEEE Transactions on Dielectrics and Electrical Insulation*, vol. 16, pp. 758-768, (2009).

[14] Vernet, J. A., Örlü, R., and Alfredsson, P. H., "Flow separation control by dielectric barrier discharge plasma actuation via pulsed momentum injection," *AIP Advances*, vol. 8, pp. 075229, (2018).

[15] Moreaua, E., Cazourb, J. and Benard, N., "Influence of the air-exposed active electrode

shape on the electrical, optical and mechanical characteristics of a surface dielectric barrier discharge plasma actuator," *Journal of Electrostatics,* vol. 93, pp. 146-153, (2018).

[16] Ebrahimi, A., Hajipour, M. and Ghamkhar, K., "Experimental study of stall control over an airfoil with dual excitation of separated shear layers," *Aerospace Science and Technology,* vol. 82, pp. 402-411, (2018).

[17] Smith, B.L. and Glezer, A., "The formation and evolution of synthetic jets," *Physics of Fluids,* vol. 10, pp. 2281–2297, (1998).

[18] Glezer, A. and Amitay, M., "Synthetic jets," *Annual Review of Fluid Mechanics,* vol. 34, pp. 503–29, (2002).

[19] Smith, B.L and Swift, G.W, "A comparison between synthetic jets and continuous jets," *Experiments in Fluids,* vol. 34, pp. 467-472, (2003).

[20] Iuso, G. and Cicca, G.M., "Interaction of synthetic jets with a fully developed turbulent channel flow," *Journal of Turbulence,* vol. 8(11), pp. 044701, (2007).

[21] Lee, C., Guang Hong, Ha, Q. P., and Mallinson, S. G., "A piezoelectrically actuated micro synthetic jet for active flow control," *Sensors and Actuators A,* vol. 108, pp. 168-174, (2003).

[22] Ariffin, A.H. and Ahmad, K.A., "Computational fluid dynamic (CFD) simulation of synthetic jet cooling: a review," *Journal of Advanced Research in Fluid Mechanics and Thermal Sciences,* vol. 2, pp. 103-112, (2020).

[23] Husin, A., Abdullah, M. Z., Ismail, A., Janvekar, A. A., Rusdi, M. S., and Ali, W. M. A. W. M., "Heat transfer performance of a synthetic jet generated by diffuser-shaped orifice," *Journal of Advanced Research in Fluid Mechanics and Thermal Sciences,* vol. 53, pp. 122-128, (2019).

[24] Yadav, H., Joshi, A., Chaudhari, M. and Agrawal, A., "An experimental study of a multi-orifice synthetic jet with application to cooling of compact devices," *AIP Advances,* vol. 9, no. 12, pp. 125108, (2019).

[25] Honohan, A.M., Amitay, M. and Glezer, A., "Aerodynamic control using synthetic jets," *AIAA Fluids 2000 Conference and Exhibit,* (2000).

[26] Hwang, W. and Eaton, J.K., "Creating homogeneous and isotropic turbulence without a mean flow," *Experiments in Fluids,* vol. 36, pp. 444-454, (2004).

[27] Variano, E.V., Bodenschatz, E. and Cowen, E.A., "A random synthetic jet array driven turbulence tank," *Experiments in Fluids,* vol. 37, pp. 613-615, (2004).

[28] Amitay, M., Honohan, A., Trautman, M. and Glezer, A., "Modification of the Aerodynamic Characteristics of Bluff Bodies Using Fluidic Actuators," *AIAA Meeting Paper, 28th Fluid Dynamics Conference,* (1997).

[29] Crook, A., Sadri, A. M. and Wood, N. J., "The development and implementation of synthetic jets for control of separated flow," *AIAA Meeting Paper, 17th Applied Aerodynamics Conference,* (1999).

[30] Chen, Y., Liang, S., Aung, K., Glezer, A. and Jagoda, J., "Enhanced mixing in a

simulated combustor using synthetic jet actuators," *AIAA Meeting Paper, 37th Aerospace Sciences Meeting and Exhibit,* (1999).

[31] Lyubimov, D. A. and Potekhina, I. V., "Application of the RANS/ILES method in analyzing the efficiency of the control of separation flows in diffusers using synthetic jets," *Fluid Dynamics,* vol. 50, no. 4, pp. 590-599, (2015).

[32] Zhao, G. and Zhao, Q., "Wind-tunnel tests of synthetic jet control efects on airfoil fow separatoin," *Scientific reports,* vol. 12, pp. 21994, (2022).

[33] Yuura, S., Watanabe, Y., Furutani, K. and Handa, T., "Ultrasonic-driven synthetic-jet actuator: High-efficiency actuator creating high-speed and high-frequency pulsed jet," *Sensors and Actuators : A. Physical,* vol. 353, pp. 114231, (2023).

[34] Crittenden, T.M. and Glezer, A., "A high-speed, compressible synthetic jet," *Physics of Fluids,* vol. 18, no. 1, pp. 017107, (2006).

[35] Pudsey, A.S., Wheatley, V. and Boyce, R.R., "Behavior of multiple-jet interactions in a hypersonic boundary layer," *Journal of Propulsion and Power,* vol. 31, no. 1, pp. 144-155, (2015).

[36] Nasr, A. and Lai, J.C.S., "Comparison of flow characteristics in the near field of two parallel plane jets and an offset plane jet," *Physics of Fluids,* vol. 9, pp. 2919–31, (1997).

[37] Ghahremanian, S., Svensson, K., Tummers, M.J. and Moshfegh, B., "Near-field mixing of jets issuing from an array of round nozzles," *International Journal of Heat and Fluid Flow,* vol. 47, pp. 84–100, (2014).

[38] Laban, A., Aleyasin, S.S., Tachie, M.F. and Koupriyanov, M., "Experimental investigation of nozzle spacing effects on characteristics of round twin free jets," *Journal of Fluids Engineering,* vol. 141, pp. 071201, (2019).

[39] Zhou, Y., Nagata, K., Sakai, Y. and Watanabe, T., "Dual-plane turbulent jets and their non-Gaussian velocity fluctuations," *Physical Review Fluids,* vol. 3, no. 12, pp. 124604, (2018).

[40] Ali, M.Y. and Alvi, F., "Jet arrays in supersonic crossflow — An experimental," *Physics of Fluids,* vol. 27, pp. 126102, (2015).

[41] Yaacob, M. R., Schlander, R. K., Buchhave, P. and Velte, C. M., "Experimental evaluation of Kolmogorov's -5/3 and 2/3 power laws in the developing turbulent round jet," *Journal of Advanced Research in Fluid Mechanics and Thermal Sciences,* vol. 45, no. 1, pp. 14-21, (2018).

[42] Bisoi, M., Das, M.K, Roy, S. and Patel, D.K., "Turbulent statistics in flow field due to interaction of two plane parallel jets," *Physics of Fluids,* vol. 29, pp. 125108, (2017).

[43] Zhou, Y., Nagata, K., Sakai, Y., Watanabe, T., Ito, Y. and Hayase, T., "Energy transfer in turbulent flows behind two side-by-side square cylinders," *Journal of Fluid Mechanics,* vol. 903, pp. 1-31, (2020).

[44] Zhou, Y., Nagata, K., Sakai, Y., Watanabe, T., "Extreme events and non-Kolmogorov -5/3 spectra in turbulent flows behind two side-by-side square cylinders," *Journal of Fluid Mechanics,* vol. 874, pp. 677-698, (2019).

[45] Smith, B.L., Trautman, M.A. and Glezer, A., "Controlled interactions of adjacent synthetic jets," *37th AIAA Aerospace Sciences Meeting and Exhibit*, (1999).

[46] Jabbal, M., Liddle, S., Potts, J. and Crowther, W., "Development of design methodology for a synthetic jet actuator array for flow separation control applications," *Journal of Aerospace Engineering*, vol. 227, pp. 110-124, (2011).

[47] Jankee, G.K. and Ganapathisubramani, B., "Interaction and vectoring of parallel rectangular twin jets in a turbulent boundary layer," *Physical Review Fluids*, vol. 6, pp. 044701, (2021).

[48] Zhang, M., Yu, Y., Simon, T.W., Cui, T., Yeom, Taiho., Huang, L. and North, M.T., "Development of synthetic jet arrays for heat transfer enhancement in air-cooled heat sinks for electronics cooling," *Proceedings of the ASME 2012 Summer Heat Transfer Conference*, pp. 601-606, (2012).

[49] Gilarranz, J.L., Traub, L.W. and Rediniotis, O.K., "A new class of synthetic jet actuators -part I: design, fabrication and bench top characterization," *Journal of Fluids Engineering*, vol. 127, pp. 367-376, (2005).

[50] Gilarranz, J.L., Traub, L.W. and Rediniotis, O.K., "A new class of synthetic jet actuators—part II: application to flow separation control," *Journal of Fluids Engineering*, vol. 127, pp. 377-387, (2005).

[51] Lyu, Y., Zhang, J., Tang, C. and Tan, X., "Temperature-variation effect of piston-driven synthetic jet and its influence on definition of heat transfer coefficient," *International*

Journal of Heat and Mass Transfer, vol. 152, p. 119347, (2020).

[52] Jacob, A., Shafi, K.A. and Roy, K.E.R., "Heat transfer characteristics of piston-driven synthetic jet," *International Journal of Thermofluids,* vol. 11, pp. 100104, (2021).

[53] Sakakibara, H., Watanabe, T., and Nagata, K., "Supersonic piston synthetic jets with single/multiple orifice," *Experiment in Fluids,* vol. 59, pp. 1-12, (2018).

[54] Eri, Q., Hong, L. and Li, T., "Novel piston-type synthetic jet actuator with auxiliary air inlet," *Journal of Aerospace Engineering,* vol. 32, no. 1, (2019).

[55] Yamamoto, K., Watanabe, T. and Nagata, K., "Turbulence generated by an array of opposed piston-driven synthetic jet actuators," *Experiments in Fluids,* vol. 63, (2022).

[56] Yamamoto, K., Ishida, T., Watanabe, T. and Nagata, K., "Experimental and numerical investigation of compressibility effects on velocity," *Physics of Fluids,* vol. 34, no. 5, pp. 055101, (2022).

[57] Ziade, P., Feero, M.A., and Sullivan, P.E., "A numerical study on the influence of cavity shape on synthetic jet performance," *International Journal of Heat and Fluid Flow,* vol. 74, pp. 187-197, (2018).

[58] Ozawa, T., Lesbros, S., and Hong, G., "LES of synthetic jets in boundary layer with laminar separation caused by adverse pressure gradient," *Computers & Fluids,* vol. 39, pp. 845–858, (2010).

[59] Ma, X., Guo, H., Fan, Z., and Zhang, L., "Investigating of simulation methods for

synthetic jet," *Procedia Engineering,* vol. 31, pp. 416 – 421, (2012).

[60] Rizzetta, D.P, Visbal, M.R., and Stanek, M.J., "Numerical investigation of synthetic-jet flow fields," *AIAA JOURNAL,* vol. 37, (1999).

[61] Guo, D. and Kral, L.D., "Numerical Simulation of the Interaction of Adjacent Synthetic Jet Actuators," *AIAA Conference and Exhibit,* (2000).

[62] Esnault, S., Duchaine, F., Gicquel, L. and Moreau, S., "Large eddy simulation of heat transfer within a multi-perforation synthetic jets configuration," *Journal of Turbomachinery,* vol. 142, no. 6, pp. 061010, (2020).

[63] Traub, L. W., Sweet, M., and Nilssen, K., "Evaluation and characterization of a lateral synthetic jet actuator," *Journal of Aircraft,* vol. 49, pp. 1039-50, (2012).

[64] Qayoum, A. and Malik, A., "Influence of the excitation frequency and orifice geometry on the fluid flow and heat transfer characteristics of synthetic jet actuators," *Fluid Dynamics,* vol. 54, no. 4, pp. 575-589, (2019).

[65] "OpenFOAM, Ver.7 For Ubuntu 16.04LTS, 8th Jul.," (2019).

[66] Zhao, M., Bian, Y., Li, Q. and Ye, T., "Large eddy simulation of transverse single/double jet in supersonic," *Aerospace Science and Technology,* vol. 89, pp. 31-45, (2019).

[67] Caretto, L. S., Gosman, A. D., Patankar, S. V. and Spalding, D. B., "Two calculation procedures for steady, three-dimensional flows with recirculation," *Proceedings of the Third International Conference on Numerical Methods in Fluid Mechanics,* vol. 19, pp.

60-68, (1972).

[68] Issa, R. I., "Solution of the implicitly discretised fluid flow equations by operator-splitting," *Journal of Computational Physics,* vol. 62, pp. 40-65, (1985).

[69] Holzmann, T., "Mathematics, numerics, derivations and OpenFOAM®," *Loeben, Germany,* (2016).

[70] Chaudhari, M., Puranik, B., Agrawal, A., "Effect of orifice shape in synthetic jet based impingement cooling," *Experimental Thermal and Fluid Science,* vol. 34, pp. 246-256, (2010).

[71] Anderson, J.D., "Modern compressible flow: with historical perspective," (1990).

[72] Yaacob, M. R., Schlander, R. K., Buchhave, P., and Velte, C. M., "A novel laser doppler anemometer (LDA) for high-accuracy turbulence measurements," *Journal of Advanced Research in Applied Sciences and Engineering Technology,* vol. 28, pp. 256-274, (2022).

[73] Takahashi, M., Fukui, R., Tsujimoto, K., Ando, T. and Shakouchi, T., "Helical structures in a temporally developing round jet in the developed state Flow," *Turbulence and Combustion,* vol. 111, pp. 1-21, (2023).

[74] Kim, M., Lee, H., Hwang, W., "Experimental study on the flow interaction between two synthetic jets emanating from a dual round orifice," *Experimental Thermal and Fluid Science,* vol. 126, pp. 110400, (2021).

[75] Wang, L. and Feng, L., "The interactions of rectangular synthetic jets with a laminar

cross-flow," *Journal of Fluid Mechanics,* vol. 899, pp. A32, (2020).

[76] Milannovic I.M., "Synthetic jets in crossflow," *AIAA Journal,* vol. 43, no. 5, pp. 929-940, (2005).

[77] Ho, H.H., Essel, E.E. and Sullivan, P.E., "The interactions of a circular synthetic jet with a turbulent crossflow," *Physics of Fluids,* vol. 34, no. 7, pp. 075108, (2022).